https://doi.org/10.5194/egusphere-2026-7174
Preprint. Discussion started: 24 November 2026
© Author(s) 2026. CC BY 4.0 License.

Bright-band detection via radial reflectivity profiles from volume-scanning radar: validation by MRR-derived melting-layer events

Hasan Hosseini[1,2], Hossein Hashemi[2], Daniel Johnson[1], Jonas Olsson[1,2], Remco van de Beek[1], Ronny Berndtsson[2], Günther Haase[1], Heiner Körnich[1]

[1]Swedish Meteorological and Hydrological Institute, Norrköping, 601 76, Sweden
[2]Division of Water Resources Engineering, Lund University, Lund, Box 118, 221 00, Sweden

Correspondence to: Hasan Hosseini (hasan.hosseini@smhi.se)

Abstract. Melting snowflakes can enhance radar reflectivity and substantially bias quantitative precipitation estimation (QPE). The atmospheric melting layer is detectable from vertical reflectivity profiles exhibiting a bright band (BB), characterized by a reflectivity peak bounded by positive and negative gradient maxima. This study extends this method using radial reflectivity profiles derived from ground-based volume-scanning weather radar (WR) and compares the results with those derived from Contoured Frequency by Altitude Diagrams (CFADs), with both approaches validated against reference melting-layer events derived from a Micro Rain Radar (MRR) in Lund, Sweden (2021–2025). 5-min full-volume WR reflectivity is reconstructed into MRR-aligned vertical profiles per radial using maximum and 90th-percentile values, while CFAD-based mode, median, and envelope profiles are derived by combining all WR volumes within an event. For radial profiles, event-mean BB characteristic heights could be compared between the MRR and the nearest C-band WR, located 76 km apart, for nearly 97 % of the reference events with available WR observations. Maximum-reflectivity profiles along the WR radial toward the MRR yielded the strongest agreement, with correlation coefficients of 0.86–0.88 and mean absolute errors of 163–172 m. CFAD-based methods produced fewer valid cases for comparison, and different methods performed best for BB peak and boundary heights. For azimuthally stratiform cases, seasonal 5-min BB height distributions showed good agreement, and WR-based QPE exhibited the greatest bias variability within the BB relative to surface observations. These results demonstrate the potential of radial reflectivity profiles for operational BB detection and quality control of QPE.

1 Introduction

The relatively narrow layer in the atmosphere where solid snowflakes transition to liquid raindrops is known as the melting layer. Most precipitation events in mid-to-high latitudes and about one third of those in the tropics are estimated to originate from melting snow aloft (Field and Heymsfield, 2015). Reflectivity-based quantitative precipitation estimation (QPE) can be substantially biased around this layer because hydrometeor size and dielectric properties change during melting. Melting snowflakes often produce reflectivity values far exceeding those of the resulting raindrops below, leading to overestimation for echoes within the melting layer. Conversely, dry snowflakes above the melting layer generally produce lower reflectivity, which can contribute to underestimation when a standard reflectivity–rainfall relationship is applied. Processes associated with

https://doi.org/10.5194/egusphere-2026-7174
Preprint. Discussion started: 24 November 2026
© Author(s) 2026. CC BY 4.0 License.

the melting layer can also introduce additional QPE uncertainties through changes in drop size distribution (DSD) and path-integrated attenuation. Detecting the melting layer is therefore important for identifying and mitigating associated QPE errors (Hosseini et al., 2025). In addition, melting-layer properties can support precipitation nowcasting in high-altitude areas, where estimating the snowfall limit is challenging (Fehlmann et al., 2018).

Melting normally begins just below the freezing level. The 0°C isotherm can be estimated from radiosonde temperature profiles (e.g., Cha et al., 2009; Di Girolamo et al., 2012; Wang et al., 2017) or lapse-rate models based on surface measurements (e.g., Fehlmann et al., 2018; Schauwecker et al., 2017). However, radiosonde observations are sparse in time and space. In addition, depending on the thermodynamic and microphysical conditions, melting layer estimates based on temperature profiles can remain uncertain. For example, sub-saturated melting layers tend to be thicker than saturated ones (Poirier et al., 2019), and sublimation cooling can delay the onset of melting (Mitra et al., 1990). Additional uncertainty arises from variations in snow particle size, shape, and density, and interactions such as collision, breakup, aggregation, and coalescence (Cha et al., 2009). Conversely, in the absence of ice-nucleating particles, liquid precipitation may persist at below 0 °C as supercooled droplets.

As an alternative, the sharp increase and decrease in the vertical gradient of reflectivity around the reflectivity peak provide useful diagnostic information for identifying the melting layer (e.g., Cao et al., 2022; Cha et al., 2009; Rajasekharan Nair, 2019). Such information is most reliably obtained from ground-based vertically pointing radar profilers, which provide continuous and vertically consistent observations (Hosseini et al., 2025). However, these observations are limited to a single atmospheric column, and the profilers are primarily used for research rather than operational networks. Vertically pointing birdbath scans from volume-scanning weather radars (WRs) can also provide columnar observations, but they are typically used for polarimetric calibration and are not usually available in single-polarization operations.

Operational WRs routinely scan at multiple lower elevation angles to provide coverage over large areas. They are therefore particularly relevant for the development and evaluation of melting layer detection methods where vertical observations are available as reference data. The volume-scanning WRs provide observations at regular time intervals, typically every 5–10 min. However, their spatial sampling is inherently uneven. Close to the radar, the beams are naturally narrower and remain closer to the surface. With increasing range, the beams broaden and rise due to their elevation angle and Earth curvature, yielding coarser vertical resolution and sampling a deeper atmospheric column whose lower edge is located at a higher altitude. Atmospheric refraction can further affect radar beam propagation and height.

Consequently, unsampled regions occur both below the lowest beam and above the highest beam. In addition, sparse elevation-angle sampling can leave gaps between vertical observations above a given surface point, whereas scanning too many elevation angles is usually impractical. Therefore, melting-layer detections from radar profilers may not always be captured by WR observations above the same site (Brast and Markmann, 2020). During widespread stratiform precipitation the bright band (BB) signature may appear in horizontal projections from a single elevation angle (e.g., Hosseini et al., 2025; Pfaff et al., 2014). However, combining reflectivity data from multiple elevation angles over a time period, e.g., in the form of Contoured Frequency by Altitude Diagrams (CFADs), i.e., two-dimensional histograms of reflectivity frequency as a function of height

https://doi.org/10.5194/egusphere-2026-7174
Preprint. Discussion started: 24 November 2026
© Author(s) 2026. CC BY 4.0 License.

(e.g., Cao et al., 2022; Goenka et al., 2023; Raut et al., 2021; Song et al., 2021; Zhou et al., 2024), suggests potential for improved melting-layer detection using WR observations.

The present study investigates the detection of BB heights from WR radial reflectivity profiles, which combine reflectivity observations sampled along individual radials (fixed azimuths) at each time step, and compares this approach with CFAD-based methods combining data from all azimuths over a time period. The radial approach makes it possible to assess the homogeneity of BB heights across azimuths and identify azimuthally stratiform cases from a single time step, thereby the risk of misidentifying temporary reflectivity enhancements caused, e.g., by artefacts, as melting-layer signatures are reduced. Specifically, the study addresses four main questions: (1) how accurately can BB heights be estimated using operational C-band WR (CWR) observations relative to reference BB events derived from a vertically pointing K-band Micro Rain Radar (MRR); (2) how does the performance of BB estimates from radial profiles compare with that of CFAD-derived profiles; (3) how can rise–fall segmentation of vertical reflectivity profiles, based on paired significant positive and negative gradients, provide additional structural information to support primary detections based on gradient maxima and the reflectivity peak; and (4) how are CWR-based QPE biases distributed below, within, and above the melting layer relative to surface observations from multiple rain-gauge stations located between the CWR and the MRR?

2 Methods and data

To address the study questions, reference melting-layer events were first derived from vertically pointing MRR observations in southern Sweden. Several bright-band detection methods were then applied to reflectivity data from a CWR located 76 km from the MRR. These methods included approaches based on radial vertical profiles and on CFAD-derived profiles. All data, methods, and procedures used to compare the resulting WR-based BB heights with the corresponding MRR-based reference values, as well as the ground validations using rain-gauge observations are described in the following sub-sections.

2.1 Linear and logarithmic reflectivity

Reflectivity is the primary radar variable for QPE, particularly for single-polarization radars. It represents the power of the backscattered signal and increases with both particle size and dielectric factor ($|K|^2$). The reflectivity enhancement in the melting layer arises from water-coated snowflakes, whose dielectric factor approaches that of liquid water, i.e., $|K|^2 \approx 0.93$, nearly 4.7 times larger than that of unit-density ice (Atlas et al., 1990), and from their generally larger sizes compared with the raindrops they eventually melt into (e.g., Fujiyoshi, 1986; Heymsfield et al., 2015).

Reflectivity Z typically follows a sixth-power dependence on particle diameter D; i.e., $Z \propto D^6$. This relationship holds in the Rayleigh-scattering regime, where D is much smaller than the radar wavelength λ, a condition generally satisfied for WRs operating at S-band ($\lambda \approx 10$ cm), C-band ($\lambda \approx 5$ cm), and X-band ($\lambda \approx 3$ cm). Enhanced reflectivity due to melting particles is also observed with radar profilers such as K-band ($\lambda \approx 13$ mm) MRRs (Hosseini et al., 2025) and Ka-band ($\lambda \approx 8$ mm) cloud radars (e.g., Di Girolamo et al., 2012; Wang et al., 2021), but not with W-band ($\lambda \approx 3$ mm) radars (Kollias and Albrecht, 2005).

https://doi.org/10.5194/egusphere-2026-7174
Preprint. Discussion started: 24 November 2026
© Author(s) 2026. CC BY 4.0 License.

Notably, the melting layer detection based on radial profiles relied on linear reflectivity Z (in $mm^6\ m^{-3}$), while the CFAD-based methods used the logarithmic decibel transformation:

$$dBZ = 10\, log_{10}\, Z\ , \tag{1}$$

2.2 MRR data and preprocessing

Micro Rain Radar (MRR) observations were collected from an MRR-2 which is located in a weather station called Norra Verket TS, Lund, southern Sweden (Figure 1), operated by the water utility company VA Syd, and has been operational since September 5, 2021. MRR-2 is currently one of the two variants of a Frequency Modulated Continuous Wave (FMCW) K-band radar profiler produced by METEK. The other variant is named MRR-PRO. More information about these instruments, including their use for melting layer detection can be found in the review paper by Hosseini et al. (2025).

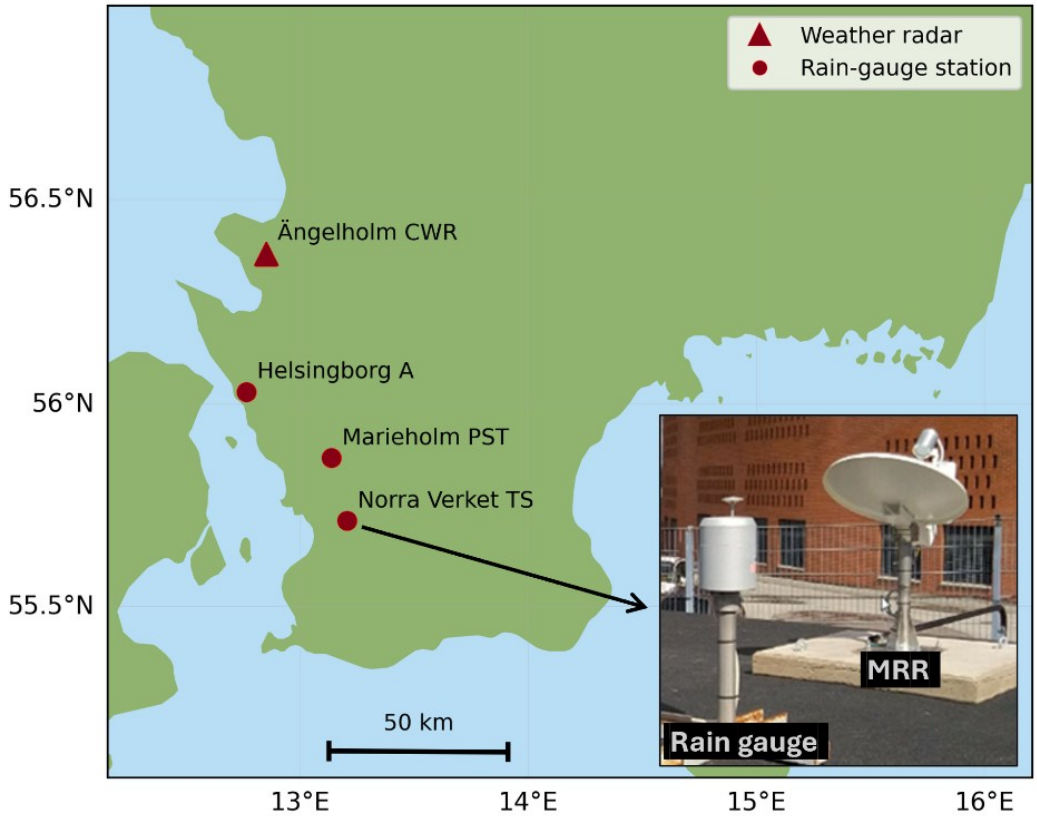

Figure 1: Location of the Norra Verket TS station hosting a Micro Rain Radar (MRR) collocated with a rain gauge, and two other rain-gauge stations located between the MRR site and the Ängelholm C-band weather radar (CWR) in southern Sweden. Map background data are from Natural Earth (https://www.naturalearthdata.com/).

https://doi.org/10.5194/egusphere-2026-7174
Preprint. Discussion started: 24 November 2026
© Author(s) 2026. CC BY 4.0 License.

In the present study, we derived vertically resolved profiles of MRR reflectivity at 1-min resolution during 2021/09/05–2025/06/30. These data were arranged as a time series of Z_1, Z_2, …, Z_N, including reflectivity data corresponding to a set of fixed range gates at heights H_i:

$$H_i = H_{MRR} + i\Delta h \qquad (i = 1, 2, \dots, N)\,, \tag{2}$$

where, H_{MRR} is MRR height that is 76 meters above mean sea level (m a.s.l), i is the height index, Δh is the MRR range resolution (=70 m), and N is number of range gates which is 31 for the MRR-2 in Lund.

These data were curated for preparing reference melting layer events. Accordingly, data from the lowest two heights (146 and 216 m a.s.l) were excluded to eliminate potential noise and clutter (Benarroch et al., 2022; Rajasekharan Nair, 2019). Therefore, the remaining n=29 MRR heights used in this study corresponded to 286, 356, …, 2246 m a.s.l. Notably, only occasional isolated missing values between two valid gates were linearly interpolated.

Profiles containing any remaining missing values were classified as invalid. In addition, profiles with reflectivity values Z < 1 $mm^6\ m^{-3}$ at the lowest useful height (here, 286 m), or profiles with fewer than five levels (out of n=29) satisfying Z > 1 $mm^6\ m^{-3}$, were also deemed invalid. These additional conditions based on the reflectivity threshold were introduced to exclude profiles unlikely to represent a precipitation column from BB analysis.

All invalid profiles were excluded, and the remaining valid profiles were processed further as described in the following sections.

2.2.1 Bright band characteristics based on peak reflectivity and gradient extrema

For every profile of Z, three bright band (BB) features could be defined, namely:

- BB bottom (BBB)
- BB peak (BBP)
- BB top (BBT)

BB peak corresponds to the height of the peak reflectivity. BB bottom and BB top were obtained from the vertical reflectivity gradients G_i, which were computed as reflectivity difference between adjacent range gates (thus, in $mm^6\ m^{-3}$ per range gate), defined as:

$$G_i = \begin{cases} Z_i - Z_{i-1}, & i = 2, 3, \dots, n \\ NaN, & i = 1 \end{cases} \tag{3}$$

Accordingly, BBB and BBT correspond to the heights of maximum positive and negative gradients, respectively. A BB defined via gradient extrema method relies on definition of three valid elements: BBB, BBP, and BBT; that is met only when the gradient extrema occurred away from the profile edges (i=1 or 29) and the height of BBP lay between that of BBB and BBT.

https://doi.org/10.5194/egusphere-2026-7174
Preprint. Discussion started: 24 November 2026
© Author(s) 2026. CC BY 4.0 License.

2.2.2 Significant rise–fall segments

The BB peaks may belong to a visibly broader segments than those defined by the BB bounds relying on the gradient extrema, and some local peaks, resembling additional BBs, may be defined by their own bounds. To consider such cases, this study applies an extended method that segments a reflectivity profile based on the distinguished rise and fall behavior.

The segmentation relied on finding significant positive and negative gradient pairs using adaptive percentile-based gradient thresholds described below. Here, "significant" refers to gradients exceeding these thresholds rather than to statistical significance; the thresholds were designed to prevent spurious detection of weak or noisy gradients. Based on empirical testing and visual inspections, the thresholds for identifying significant positive and negative gradients were initially set at the 85th percentile of the positive and negative gradient magnitudes, respectively. This percentile serves as the starting threshold and is subsequently increased, if necessary, to limit the number of detected rise–fall segments to a physically plausible maximum. To prevent unrealistically small thresholds in weak reflectivity profiles, the threshold was additionally constrained to be no smaller than 6% of the reflectivity at the lowest valid gate, a value that was likewise selected empirically.

Then, a "significant" rise and fall can occur when $G_i \geq T^+$ and $G_i \leq -T^-$, respectively, where T^+ and T^- are the percentile-based thresholds that are adaptively determined.

Starting from the lowest valid gate, the algorithm searched for the first significant positive gradient

$$s = \underset{i \in [2,n]}{arg\,min}\{G_i \geq T^+\}, \tag{4}$$

which marks the onset of a rise–fall segment. From immediately after this rise, the algorithm then searched upward for the next significant negative gradient

$$f = \underset{j>s}{arg\,min}\{G_j \leq -T^-\}, \tag{5}$$

which marks the onset of the significantly descending part of the segment. The segment endpoint was defined as the last significant negative gradient before either the next significant positive gradient or n, i.e., upper end of the profile. If p denotes the index of the next significant positive gradient, or n (if none exists), then the segment endpoint is

$$e = \underset{l \in [f,p)}{arg\,max}\{G_l \leq -T^-\}, \tag{6}$$

This alternating rise–fall search was repeated iteratively through the entire profile, producing a sequence of non-overlapping rise–fall segments [s_k, e_k]. In this way, the algorithm also allowed neutral segments between the end of a rise–fall segment and the beginning of the next, as well as before the first s, and after the last e, ensuring that the segmentation covered the entire profile. However, these neutral segments are irrelevant to the BB and, hereafter, the term segment refers only to the significant rise–fall segments, which may contain either a local or the global reflectivity peak.

https://doi.org/10.5194/egusphere-2026-7174
Preprint. Discussion started: 24 November 2026
© Author(s) 2026. CC BY 4.0 License.

To avoid detecting an excessive number of segments, if the initial thresholding (85th percentile) produced more than three significant rise–fall segments, the threshold was incrementally increased until the number of detected segments fell below this prescribed limit. In practice, this procedure usually detected only one segment per profile. Sporadic multiple segments may be associated with dual melting layers (Ikeda et al., 2005; Martner et al., 2007). However, some transient segments may result from clutter. Therefore, allowing up to three segments provides a flexibility to detect situations where dual melting layers coexist with an additional clutter-induced segment, although such situations are expected to be rare. Despite this flexibility, only the segment containing the global reflectivity peak is analyzed and illustrated in the present study.

The segment containing the global reflectivity peak is primarily used for illustration. In addition, it serves as a fallback criterion for BB identification when the gradient-extrema method fails to provide stable or valid BB boundaries. This fallback procedure was applied only to the analyses of CWR radial profile. For the MRR-based BB detection, this flexibility was deliberately not adopted in order to ensure a stricter definition of the reference melting layer events.

Segments containing local reflectivity peaks, other than the global reflectivity peak, are not investigated further in this study. However, they may prove useful techniques in future studies focusing on complex vertical structures, such as dual melting layers.

2.2.3 Reference melting layer events based on MRR

A reference melting layer event was defined based on the temporal stability of the BB peak height distribution. For this purpose, the 1-min MRR profiles were aggregated into 30-min time blocks. A 30-min time block was marked as stable when both following criteria were satisfied:

- it contained a minimum number of 1-min profiles with a valid BB detection: N_v=20, and
- the peak heights within the time block satisfied a vertical coherence condition:

$$H_{BBP,P90} - H_{BBP,P10} < S, \qquad (S = c\Delta h)\,, \tag{7}$$

where *P10* and *P90* denote the 10th and 90th percentiles, Δh=70 m is the range resolution, and c is a small integer (c=3, alternatively c=2).

An event began when a stable block was encountered and could continue as long as subsequent blocks also satisfied the stability criteria. When the criteria are not met for a block, the preceding consecutive sequence of stable blocks was evaluated as a candidate melting layer event. It was saved as an event only if two global conditions are met:

- the total number of valid BB profiles across the entire event was ≥ N_v, and
- the BB peak heights across the whole event satisfied the vertical coherence presented in Eq. (7).

For each event, the heights of BBB, BBP, and BBT for every valid 1-min profile, and their event-mean values were stored as reference melting layer data. Notably, the event extraction process was also performed separately using the alternative assumptions of N_v and c. However, the presented results in this study primarily relied on N_v=20, and c=3.

https://doi.org/10.5194/egusphere-2026-7174
Preprint. Discussion started: 24 November 2026
© Author(s) 2026. CC BY 4.0 License.

Notably, a melting layer event differs from a precipitation event that is normally defined based on continuity of precipitation, rather than stability of the BB condition in this case.

2.3 Scanning weather radar volumetric data used for BB detection

The Swedish Meteorological and Hydrological Institute (SMHI) operates a nationwide network of CWR systems. Under the current operational configuration, each CWR performs a full volumetric scan every five minutes using a set of ten elevation angles 0.5°, 1°, 1.5°, 2°, 2.5°, 4°, 8°, 14°, 24°, and 40°. At each elevation angle, the antenna completes a full 360° azimuthal rotation, producing one scan composed of 360 rays. Reflectivity is sampled over several hundred range gates along each ray with a constant range resolution variable across scans.

Table 1 summarizes the range-gate configuration for each elevation angle, together with the corresponding maximum slant range, ground distance, and beam-center height. The geometric quantities are calculated assuming a spherical Earth and straight-line radar beam propagation, i.e., without atmospheric refraction. This idealized geometry, particularly used for the radial BB detection method, provides a geometric reference against which deviations in BB height estimates can be interpreted. In particular, underestimation and overestimation of BB height relative to the MRR reference may partly be attributed to sub-refraction and super-refraction, respectively, provided that other sources of discrepancy, such as horizontal BB variability, beam broadening, and sampling-volume effects, are small. This interpretation also assumes that the vertically pointing MRR observations are only negligibly affected by atmospheric refraction.

Table 1. Specifications of the SMHI's C-band weather radar range-gate sampling and the corresponding maximum ground distance and beam-center altitude for the adopted elevation angles. Distances and heights were computed assuming a spherical Earth and straight-line propagation, i.e., without atmospheric refraction.

Elevation angle (°)	Gates per ray	Range gate resolution (m)	Max slant range (km)	Max ground distance (km)	Max beam height (km)
0.5	480	500	240	239.8	6.6
1.0	480	500	240	239.7	8.7
1.5	480	500	240	239.6	10.8
2.0	480	500	240	239.4	12.9
2.5	592	250	148	147.7	8.17
4.0	592	250	148	147.4	12.0
8.0	592	250	148	146.1	22.3
14.0	592	250	148	142.8	37.4
24.0	480	250	120	108.8	49.7
40.0	480	250	120	90.8	77.8

https://doi.org/10.5194/egusphere-2026-7174
Preprint. Discussion started: 24 November 2026
© Author(s) 2026. CC BY 4.0 License.

According to ground distances, observations from all elevation angles are simultaneously available only within approximately 91 km of the radar, according to the highest elevation angle (40°). In southern Sweden, precipitating clouds are not expected to exceed a 10–12 km a.s.l height, near the tropopause, except during rare episodes of deep overshooting convection that may inject ice particles and water vapor into the lower stratosphere (Konjari et al., 2025). At the two highest elevation angles (24° and 40°), the radar beams reach the upper troposphere over much shorter ground distances (~10–25 km), where they generally provide little or no information on precipitation. In contrast, the four lowest elevation angles (0.5°–2°) remain below the tropopause over much larger ground distances, extending to approximately 240 km. For elevation angles of 2.5° and 4°, this coverage decreases to about 147 km, and for higher elevation angles of 8° and 14° it is further reduced to roughly 40–75 km. Given this distance–height sampling distribution and considering that the melting layer can occur well below the tropopause, bright band analyses based on volumetric radar data become less representative at larger ground distances from the radar. Consequently, melting layer events derived from the MRR are considered reliable reference cases only for WRs located at intermediate distances from the MRR, where the melting layer is adequately sampled by the radar volume. Among the surrounding CWRs, only the Ängelholm radar satisfies these criteria, being located 76 km from the MRR site (CWR azimuth 163°), whereas the second-closest radar lies far beyond the aforementioned 91-km range where observations from all elevation angles are available. Therefore, the scanning radar analyses presented in this study are based on the Ängelholm CWR.

Two methods were evaluated for BB detection: one based on analyses along individual radials, and the other exploiting the full volumetric data set through CFAD-based profiles. Notably, the 5-min CWR data files used in the present study include quality-controlled reflectivity data which are operationally produced using the BALTRAD software (BALTRAD · GitHub, 2025). The quality control comprised of a clutter and anomaly detection and removal ("bROPO"), and a correction for beam blockage caused by topography ("beamb").

The data were available in HDF5 files with a unified format following the EUMETNET ODIM H5 standard with different versions used over the years (Michelson et al., 2024), and were obtained for each MRR-derived event period. Reflectivity data included two types of flagged values: “undetect”, indicating measurements below the detection threshold (i.e., radiated but nothing detected), and “nodata”, indicating missing measurements (i.e., never radiated). In the CFAD-based method, both “undetect” and “nodata” values were excluded. In the radial-profile method, “nodata” values were also excluded, while “undetect” values were assigned a nominal value of −40 dBZ. This approach helped retain more reflectivity values in the reconstructed radial profiles, given the more limited sampling along individual radials at each time step compared with the CFAD-based method, which combines observations from all azimuths over multiple time steps. More in the following.

Note that, all time references in this study are given in Coordinated Universal Time (UTC).

2.4 CWR-based BB detection using radial reflectivity profiles

To ensure vertically consistent-sampled profiles based on CWR, only complete radar volumes, i.e., volumes containing data from all ten elevation angles, were retained. Time steps with missing scans were excluded. All subsequent processing relied exclusively on linear reflectivity Z.

https://doi.org/10.5194/egusphere-2026-7174
Preprint. Discussion started: 24 November 2026
© Author(s) 2026. CC BY 4.0 License.

2.4.1 Common azimuth–height grid

Due to azimuthal misalignment among elevation scans, a common azimuth grid consisting of 360 one-degree bins centered at 0.5°, 1.5°, …, 359.5°, was defined for the BB analyses, and reflectivity measurements from the native radar rays were assigned to the nearest azimuth bin. For each volume, the reflectivity data were then mapped from polar coordinates (azimuth, range, and elevation) to a fixed azimuth–height grid, with a vertical spacing Δh=70 m consistent with the MRR height sampling. This common grid enabled reconstruction of radial reflectivity profiles, as shown in Figure 2 and described further below.

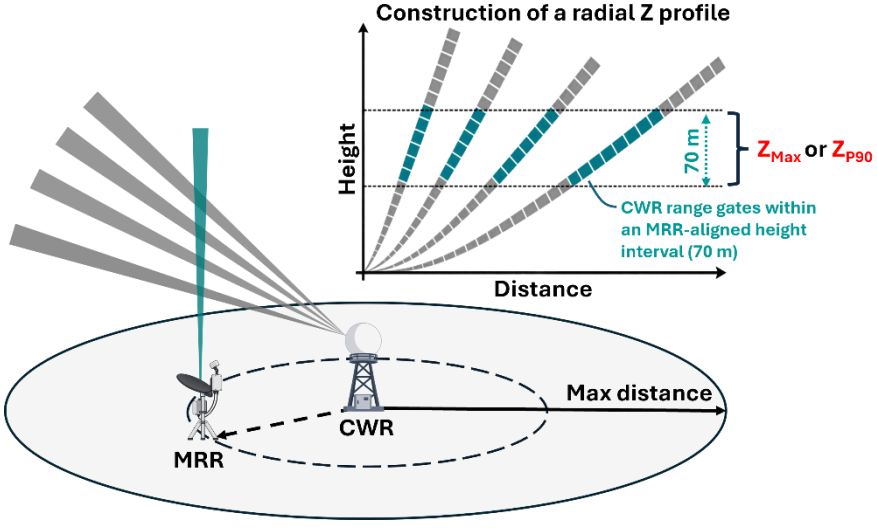

Figure 2: Schematic of constructing MRR-aligned radial reflectivity profiles for C-band weather radar (CWR).

The minimum height H_{min} was defined as the lowest MRR-equivalent height located at least $2\Delta h$ above the CWR antenna height h_{cwr}. The maximum height H_{max} was determined by applying a 5% buffer to the highest MRR gate height and rounding up to the nearest higher 70-m grid level. Consequently, the CWR azimuth–height grid was constructed on the MRR-aligned heights, starting at H_{min}, with the upper limit H_{max} which extends slightly beyond MRR range. For the Ängelholm CWR, with h_{cwr} = 209 m a.s.l, H_{min} and H_{max} are 356 and 2386 m a.s.l, respectively (Table A1).

For each azimuth bin, slant range gates were first restricted to those whose beam-center heights lay within the vertical range extended by $0.5\Delta h$ from both ends, and then, each retained gate was assigned to the nearest MRR-aligned height bin (H_k):

$$H_k = \min_{H \in (H_{min}-0.5\Delta h,\, H_{max}+0.5\Delta h)} |h(r,\theta) - H|\,,\ |h(r,\theta) - H_k| < \Delta h\ , \tag{8}$$

where $h(r,\theta)$ denotes the beam-center height at slant range r and elevation angle θ. For each height bin along a given radial of the Ängelhom CWR, between 28 and 43 range gates satisfied this condition (Table A1), with the highest sampling density

https://doi.org/10.5194/egusphere-2026-7174
Preprint. Discussion started: 24 November 2026
© Author(s) 2026. CC BY 4.0 License.

occurring in the low-to-mid elevation angles. This results from the longer slanted paths for the lower elevation scans, and the finer range resolution of the intermediate elevation scans, as shown in Table 1.

2.4.2 Radial profiles and BB curation

Because multiple reflectivity data can be mapped to each azimuth-height grid cell (Eq. 8), a representative reflectivity value was instead calculated and assigned. Two representative choices were based on two metrics: maximum and 90th percentile. The 360 radial profiles per representation method were processed independently for BB detection. The profiles with Z < 1 mm^6 m^{-3} at H_{min} or with fewer than five vertical levels satisfying Z > 1 mm^6 m^{-3} were deemed invalid. For the remaining valid profiles, the BB characteristics (BBB, BBP, and BBT) were initially estimated following the same procedure as for the MRR profiles. However, the availability of neighboring radial profiles enabled identification of suspicious estimates and the smoothing of BB heights across adjacent radials.

Radial outliers were identified using a z-score criterion applied across all radials at a given time step and evaluated independently for each BB height component (BBB, BBP, or BBT). For a generic BB height component $h_{bb}(\alpha)$, the standardized deviation was computed as:

$$z = \frac{h_{bb}(\alpha) - \mu_h}{\sigma_h}, \tag{9}$$

where μ_h and σ_h denote the mean and standard deviation across all radials, respectively. Radials for which $|z| > 2.5$ in any BB height component were flagged as outliers and excluded. The outlier test was applied to the raw peak and extrema-based bounds, i.e., prior to smoothing.

Radial smoothing was applied to the remaining, non-outlier radials using circular triangular weights within a fixed azimuthal sector. For each radial α, the smooth BB height was:

$$h'_{bb}(\alpha) = \frac{\sum_{d=-S/2}^{S/2} \omega(d)\, h_{bb}(\alpha+d)}{\sum_{d=-S/2}^{S/2} \omega(d)}, \quad \omega(d) = max\left(0, 1 - \frac{2|d|}{S}\right), \tag{10}$$

where index d wraps cyclically in azimuth and S denotes the full width of the smoothing sector in degrees (here, S = 6°). The resulting BB characteristics based on each representation were denoted via suitable subscripts, so: BBB_{Max}, BBB_{90th}, BBP_{Max}, BBP_{90th}, BBT_{Max}, and BBT_{90th}.

In addition to gradient extrema, significant rise–fall segmentation (identical to that applied to the MRR profiles) was used as a secondary structural descriptor for the radial profiles. When the BB boundaries derived from gradient extrema were invalid, i.e., did not contain the global reflectivity peak, the segmentation results were consulted to verify whether the peak was embedded within a coherent segment. This fallback criterion did not replace the invalid BB boundaries obtained from the gradient-extrema method but was used solely to support acceptance of the global reflectivity peak as a BB peak. As noted earlier, the fallback criterion was applied only to the CWR analyses. For the MRR, the BB peak was retained only when valid gradient-extrema boundaries were identified, ensuring a stricter definition of the reference events.

https://doi.org/10.5194/egusphere-2026-7174
Preprint. Discussion started: 24 November 2026
© Author(s) 2026. CC BY 4.0 License.

The resulting smoothed BB peak and corresponding upper and lower bounds, after radial outlier removal, acceptance check, and smoothing, were taken as the final scanning CWR-based BB indicators for each radial and time step.

2.5 CWR-based BB detection using CFAD-based profiles

Based on the time periods of each MRR-based curated event, available volumetric reflectivity data from CWR Ängelholm were binned with respect to intensity value (dBZ) and height (m a.s.l). The bins span -32–96 dBZ with 0.5 dB increment and 0–15000 m with 100 m increment. The height of each CWR observation was determined by standard atmospheric beam propagation according to the BALTRAD methods (BALTRAD · GitHub, 2025). The vertical increment and propagation method differ from those used in the radial method because the data used for the CFAD-based method were originally prepared for another purpose and were used directly here.

The resulting CFAD in the form of two-dimensional (2D) intensity–height histogram was used to calculate three statistical metrics per each height: mode, median and envelope. Mode and median were the most frequent reflectivity and the median reflectivity, respectively, whereas the envelope was defined as the maximum reflectivity. The maximum reflectivity can vary significantly in adjacent height intervals, so, prior to calculating the metrics, a threshold was applied to exclude the infrequent observations, specifically scattered high-intensity values that would have created a jagged envelope. The threshold was either an absolute count (e.g., 50) or as a fraction (e.g., 0.0005), depending on the use of absolute or relative frequencies in constructing the 2D histogram. The relative frequencies were calculated from the number of valid observations divided by the total number of possible observations in each height interval.

The three CFAD-derived metrics (mode, median, and envelope) produce distinct vertical profiles. Each profile was first interpolated to the MRR height levels, with missing values filled by linear interpolation. The interpolated profiles were then smoothed prior to gradient calculation. Smoothing was performed using weights derived from a normalized triangular kernel of width 5.

Given w an odd integer representing this width and indices $k = 0,1, \ldots, w–1$, the normalized weights

$$\omega_k = \frac{t_k}{\sum_{k=0}^{w-1} t_k}, \quad t_k = \frac{w+1-|2k-(w-1)|}{2}, \tag{11}$$

For $w = 5$, $t = [1, 2, 3, 2, 1]$, and so $\omega = [1/9, 2/9, 1/3, 2/9, 1/9]$. The interpolated profile was padded with two zeroes on both ends. The smoothing was applied as a discrete convolution between the padded profile and the normalized kernel, thereby minimizing edge effects.

After smoothing, vertical gradients were computed according to the Numpy function gradient; where, second-order central differences are applied at interior height levels, and first- or second-order one-sided differences are used at the edges (numpy.gradient — NumPy v2.2 Manual, 2026). Finally, the maximum reflectivity of each profile was defined as the BB peak, and the BB bottom and BB top were identified from the lower and upper gradient extrema, respectively. The resulting BBB feature were also named with suitable subscripts, i.e., BBB_{Mode}, BBB_{Median}, $BBB_{Envelope}$, BBP_{Mode}, BBP_{Median}, $BBP_{Envelope}$, BBT_{Mode}, BBT_{Median}, and $BBT_{Envelope}$.

https://doi.org/10.5194/egusphere-2026-7174
Preprint. Discussion started: 24 November 2026
© Author(s) 2026. CC BY 4.0 License.

As a consistency check among different methods, it was verified that the BB peak lay between BB bottom and BB top. However, it should be noted that this method did not include any calculation of significant gradients that was performed using MRR profiles and CWR-based radial profiles.

2.6 Measures for comparing BB height estimates using CWR and MRR

A combination of visual and statistical analyses was used to compare corresponding BB heights derived from CWR and MRR data. Visual agreement between paired estimates was primarily assessed using hexbin plots. Unlike conventional scatter plots, hexbin plots represent the joint distribution as a two-dimensional histogram in which the plotting area is partitioned into non-overlapping, domain-filling hexagonal cells. The color intensity of each cell reflects the number of data points within that bin, allowing clearer visualization of data density.

The statistical metrics used to quantify the performance of the CWR-based BB height estimates relative to the MRR reference are summarized in Table 2.

Pearson's correlation coefficient (PCC) measures the strength of the linear relationship between paired estimates, whereas Spearman's rank correlation coefficient (SCC) evaluates the monotonic association based on ranked values and is less sensitive to outliers. The mean absolute error (MAE) quantifies the average magnitude of deviations between CWR and MRR heights, expressed in meters, independent of direction. Percent bias (PBIAS) measures the systematic deviation of CWR estimates relative to MRR, expressed as a percentage; positive values indicate overestimation by CWR, whereas negative values indicate underestimation.

Table 2. Metrics used to evaluate agreement between BB characteristic heights derived from CWR (h') and MRR (h)

Metric	Equation	Range	Best
Pearson's correlation coefficient	$\mathrm{PCC} = \frac{\sum_{i=1}^{n}(h_i' - \bar{h'})(h_i - \bar{h})}{\sqrt{\sum_{i=1}^{n}(h_i' - \bar{h'})^2}\sqrt{\sum_{i=1}^{n}(h_i - \bar{h})^2}}$	[-1, 1]	1
Spearman's rank correlation coefficient	$\mathrm{SCC}^{a} = \frac{\sum_{i=1}^{n}[R(h_i') - \overline{R_{h'}}][R(h_i) - \overline{R_h}]}{\sqrt{\sum_{i=1}^{n}[R(h_i') - \overline{R_{h'}}]^2}\sqrt{\sum_{i=1}^{n}[R(h_i) - \overline{R_h}]^2}}$	[-1, 1]	1
Mean absolute error (m)	$\mathrm{MAE} = \frac{1}{n}\sum_{i=1}^{n}\lvert h_i' - h_i\rvert$	[0, +∞)	0
Percent bias (%)	$\mathrm{PBIAS} = 100\frac{\sum_{i=1}^{n}(h_i' - h_i)}{\sum_{i=1}^{n} h_i}$	(-∞, +∞)	0

[a] R stands for rank

https://doi.org/10.5194/egusphere-2026-7174
Preprint. Discussion started: 24 November 2026
© Author(s) 2026. CC BY 4.0 License.

2.7 Widespread stratiform samples for analysis of seasonal BB height distributions

To examine whether the CWR reproduces the seasonal BB-height distributions observed by the MRR, the probability distributions of 5-min BB heights for samples representative of stratiform precipitation were analysed. The BB is primarily associated with stratiform precipitation, whereas detections during localized convective rainfall are more uncertain. Moreover, the WR-based BB height estimates were derived by combining data from different ranges, while the reference MRR provides vertically pointing observations over a single atmospheric column. Restricting the analysis to widespread stratiform conditions therefore improves the comparability of the WR- and MRR-based BB heights at the 5-min timescale.

For each step, the variability of the retrieved BB height across radials was quantified by the coefficient of variation (COV; as the ratio of standard deviation to mean) and those with at least 30 valid radial BB-height retrievals and COV $\leq$ 0.25 were retained, consistent with a coherent melting layer under widespread stratiform conditions.

For the retained time steps, a representative BB height was obtained as a radially weighted mean of the BB height estimates within ±5° of the azimuth pointing toward the MRR location. Weights decreased linearly with increasing angular distance from the target azimuth. The reference BB height from MRR was also averaged over the corresponding 5-min interval starting at the CWR time stamp (i.e., minutes t to t+4). The resulting matched pairs of BB height estimates were then combined across all events and grouped by the three-month seasons December-January-February (DJF), March-April-May (MAM), June-July-August (JJA), and September-October-November (SON) to derive seasonal probability distributions for winter, spring, summer, and autumn in the case study.

2.8 Ground validation

To assess the representativeness of CWR reflectivity measurements obtained at different elevations relative to the bright band for estimating rainfall at the ground, radar-derived rainfall estimates were compared with observations from three rain gauges located between the Ängelholm CWR and the MRR site in Lund (Figure 1): Helsingborg A, Marieholm PST, and Norra Verket TS. Helsingborg A is equipped with a Geonor weighing gauge reporting precipitation at 15-min intervals (with a temporal resolution of up to 1 min), whereas Marieholm PST and Norra Verket TS are tipping-bucket gauges with a resolution of 0.2 mm per tip.

For consistency, all gauge observations were aggregated to 15-min totals. Radar rainfall rates were estimated directly from reflectivity using the standard Marshall–Palmer relationship, $Z=200R^{1.6}$, without applying systematic bias correction. For each 15-min period, the radar rainfall estimate at each rain-gauge location was obtained from the closest radar bin at each elevation angle and paired with the corresponding gauge observation. The rainfall bias was then analyzed as a function of the signed vertical distance between the radar-bin center and the nearest BB boundary, where negative distances indicate measurements below the BB, positive distances indicate measurements above the BB, and measurements within the BB are treated separately.

https://doi.org/10.5194/egusphere-2026-7174
Preprint. Discussion started: 24 November 2026
© Author(s) 2026. CC BY 4.0 License.

3 Results and discussions

This section presents and discusses the results of the study based on the data and methods described earlier. First, the reference melting layers derived from the MRR are presented using a statistical overview of the events. Next, several examples of BB detection from both MRR and CWR data are shown using dedicated profiles and two-dimensional histograms. Broader comparisons of CWR-based BB heights with those derived from the MRR are then presented via hexbin plots and performance metrics based on event-mean values. Furthermore, all 5-min samples classified as widespread stratiform are used to examine the seasonal probability distributions of BB height estimates from CWR and MRR, and performance metrics are also calculated and discussed for these samples. Finally, the ground validation results using rain-gauge observations are presented and discussed.

3.1 MRR-derived reference BB events

As shown in Table 3, different numbers and durations of reference events were derived using the MRR depending on the values of N_v and c (Sect. 2.2.3). Given N_v=20, c=3 compared with c=2 resulted in higher number of reference events (328 vs. 287) and longer average duration (66 vs. 54 min).

For both assumptions, at least half of the events had a 30-min duration, equivalent to the time block used for the definition of the events, and the median start time of the events was around 10:00 UTC.

Figure 3 illustrates examples of MRR reflectivity profiles from a 60-min BB event on 2021-12-31, co-detected using both assumptions of c (2 and 3) and N_v = 20, as introduced in Sect. 2.2.3.

Table 3. Summary statistics of start time and duration for MRR-derived bright-band events under two assumptions.

Assumption	n	Variable	Ave	Min	Prc5	Prc25	Med	Prc75	Prc95	Max
N_v=20, c=3	328	Start (UTC)	10:48	00:00	00:40	04:30	10:00	16:30	22:30	23:30
		Dur (min)	66 ±72[a]	30	30	30	30	90	180	810
N_v=20, c=2	287	Start (UTC)	11:18	00:00	01:00	05:15	10:30	17:00	22:30	23:30
		Dur (min)	54 ±44[a]	30	30	30	30	60	150	330

[a] Average ± standard deviation

https://doi.org/10.5194/egusphere-2026-7174
Preprint. Discussion started: 24 November 2026
© Author(s) 2026. CC BY 4.0 License.

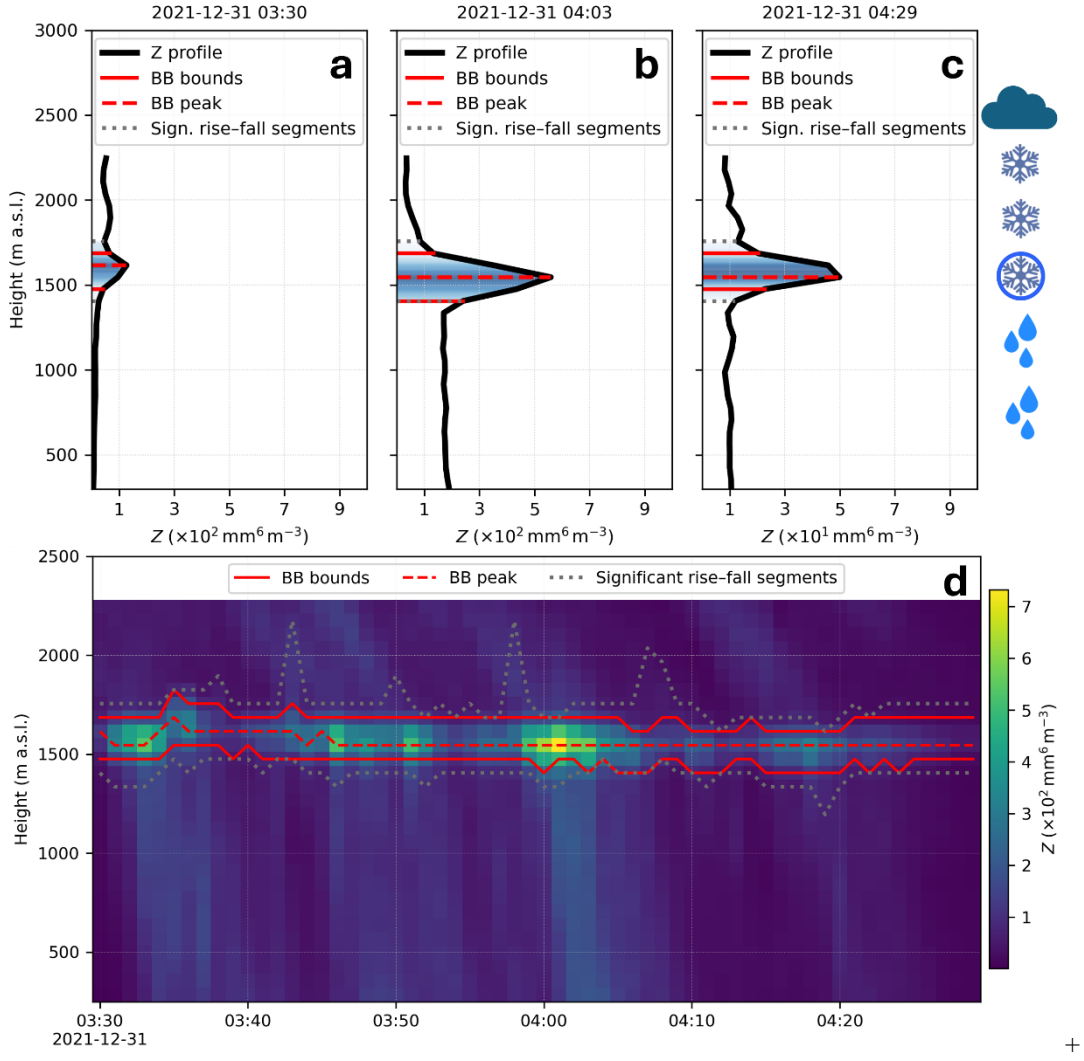

Figure 3: MRR-derived bright-band (BB) detection for an event on 31 December 2021 (03:30–04:29 UTC). The upper panels (a, b, and c) show three example reflectivity profiles (03:30, 04:03, and 04:29) with valid BB peak and bounds, together with corresponding rise–fall segmentation. The lower panel (d) shows the 1-min time series overlaid on the MRR reflectivity time–height histogram.

In the beginning of the BB event at 03:30 (Figure 3a), snow reflectivity is greater than rain reflectivity because it coincided with the beginning of a rainfall episode, when precipitation was not fully developed at surface. To clarify, snow and rain reflectivity are measured above and below of the BB top and BB bottom boundaries, respectively. Later, in the middle of the event at 04:03 (Figure 3b), when near-surface reflectivity was maximized, a typical profile of reflectivity appears where snow reflectivity is smaller than rain reflectivity. Finally, at 04:29 (Figure 3c), when near-surface reflectivity decreases again at the end of the event, BB peak and bounds are still detected at heights comparable with those of earlier times.

https://doi.org/10.5194/egusphere-2026-7174
Preprint. Discussion started: 24 November 2026
© Author(s) 2026. CC BY 4.0 License.

Figure 4 presents MRR-based BB detection for two other events on 4 February 2022 and 18 May 2025. Compared with Figure 3d, the February 2022 event (Figure 4a) is longer in duration (150 vs. 60 min), exhibits a lower BB peak height (~1000 vs. ~1500 m a.s.l.), and shows generally higher peak reflectivity (the order of 10^3 vs. 10^2 mm^6 m^{-3}).

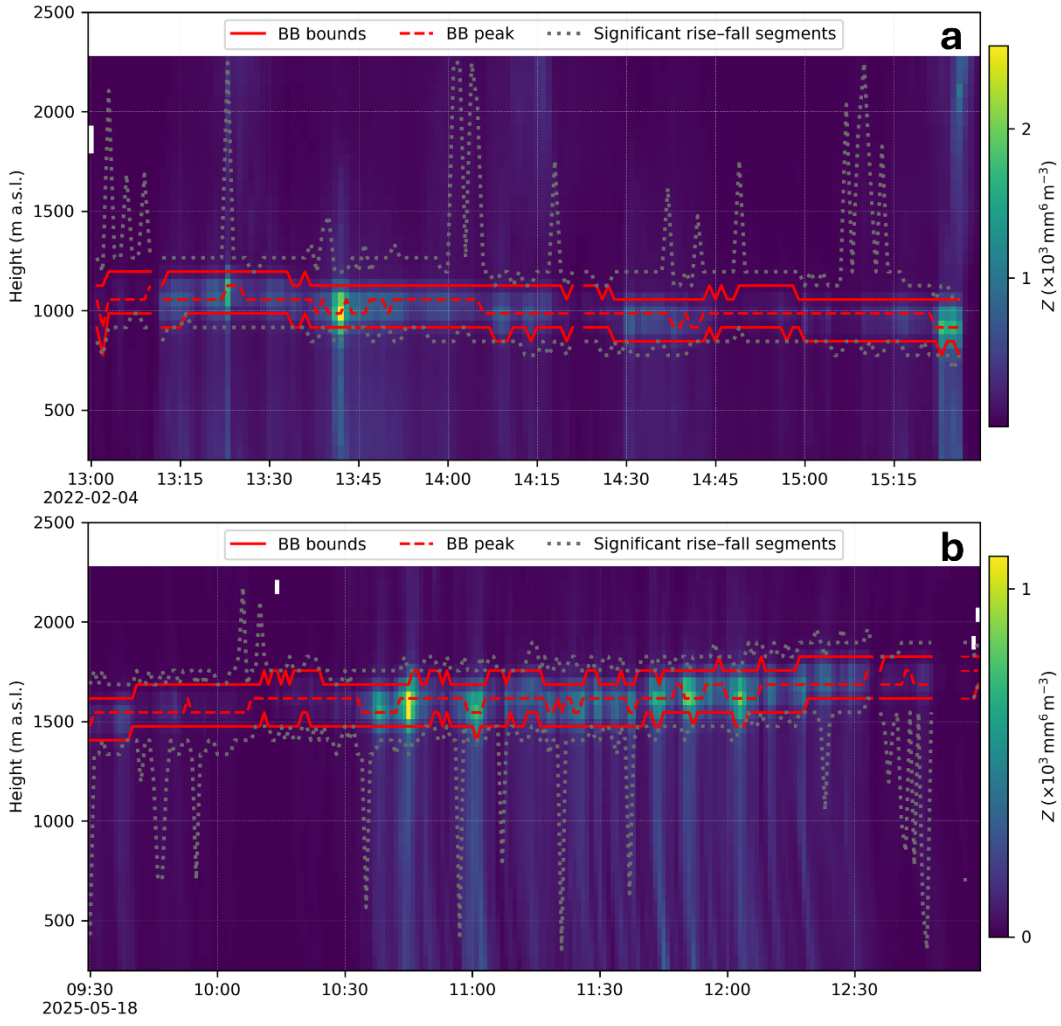

Figure 4: Same as Figure 3d, but for the events on 4 February 2022 (13:00–15:29 UTC) (a) and 18 May 2025 (09:30–12:59 UTC) (b).

Despite these differences, the BB thickness, i.e., the separation between BB top and bottom bounds, remains comparable across these events (~210 m). Similar to the winter event in Figure 3d, the event on 4 February 2022 (Figure 4a) exhibits pronounced jagged variability in the upper (i.e., fall) boundary of the rise–fall segments, resulting in intermittent large vertical offsets relative to the comparatively stable BB top height. This behavior is consistent with a gradual and heterogeneous onset of melting, where weak reflectivity gradients above the BB peak height are sensitive to microphysical variability and mixed-phase conditions, which complicate identification of the termination of the fall gradient.

https://doi.org/10.5194/egusphere-2026-7174
Preprint. Discussion started: 24 November 2026
© Author(s) 2026. CC BY 4.0 License.

In the 18 May 2025 event (Figure 4b), enhanced variability is instead more evident in the lower (i.e., rise) boundary of the rise–fall segments, while the BB bottom height remains stable. Under warmer-season conditions, short-scale reflectivity variability below the melting layer, associated with evolving rain microphysics and sub-melting layer thermodynamic effects, can influence the detection of the onset of the significant rise toward the BB peak.

Overall, rise–fall segment boundaries may exhibit enhanced variability above and below the BB peak, depending on the prevailing microphysical conditions and the assumptions of the utilized method, whereas the BB bounds derived from gradient extrema remain comparatively robust. Nevertheless, the event-mean heights of the rise–fall segment boundaries can still provide useful complementary information, as their occasional jagged behavior tends to average out over an event. In this study, rise–fall segments are used primarily for illustration, and reference BB events are defined solely based on the gradient-extrema BB bounds.

3.2 Ängelholm CWR-based BB detection using radial reflectivity profiles

Figure 5 illustrates CWR-based BB heights detected using the radial profiles based on the 90th percentile and maximum reflectivity for all 360 radials at a 5-min step starting at 14:00 for the event on 4 February 2022.

Regardless of noisier reflectivity for the maximum profiles (Figure 5a) than the 90th profile (Figure 5b), the variability of the BB heights across radials is relatively small and the BB thickness is typically 210–280 m for both. Therefore, the results are comparable with the MRR-derived results discussed earlier. However, the BB heights at the MRR (azimuth≈163˚) are underestimated compared with MRR estimates (see corresponding time in Figure 4a), due to approximated beam height for the CWR and the fact that data from various ranges are used to construct these profiles. The generally homogeneous BB heights observed across radials shown in Figure 5 was also observed during the entire period of the BB event, indicating a widespread winter stratiform precipitation event.

Figure 6 illustrates CWR-based estimates at a sample time step (11:50) of the BB event on 18 May 2025, which exhibits greater variability in BB heights across radials. In this example, interruptions in the BB height estimates occur for some radials within the 210–360° azimuthal sector when the detection criteria are not met. This azimuthal sector generally received light rainfall. It should be recalled that the evaluation of the CWR estimates focuses on the radial toward the MRR (azimuth≈163°).

https://doi.org/10.5194/egusphere-2026-7174
Preprint. Discussion started: 24 November 2026
© Author(s) 2026. CC BY 4.0 License.

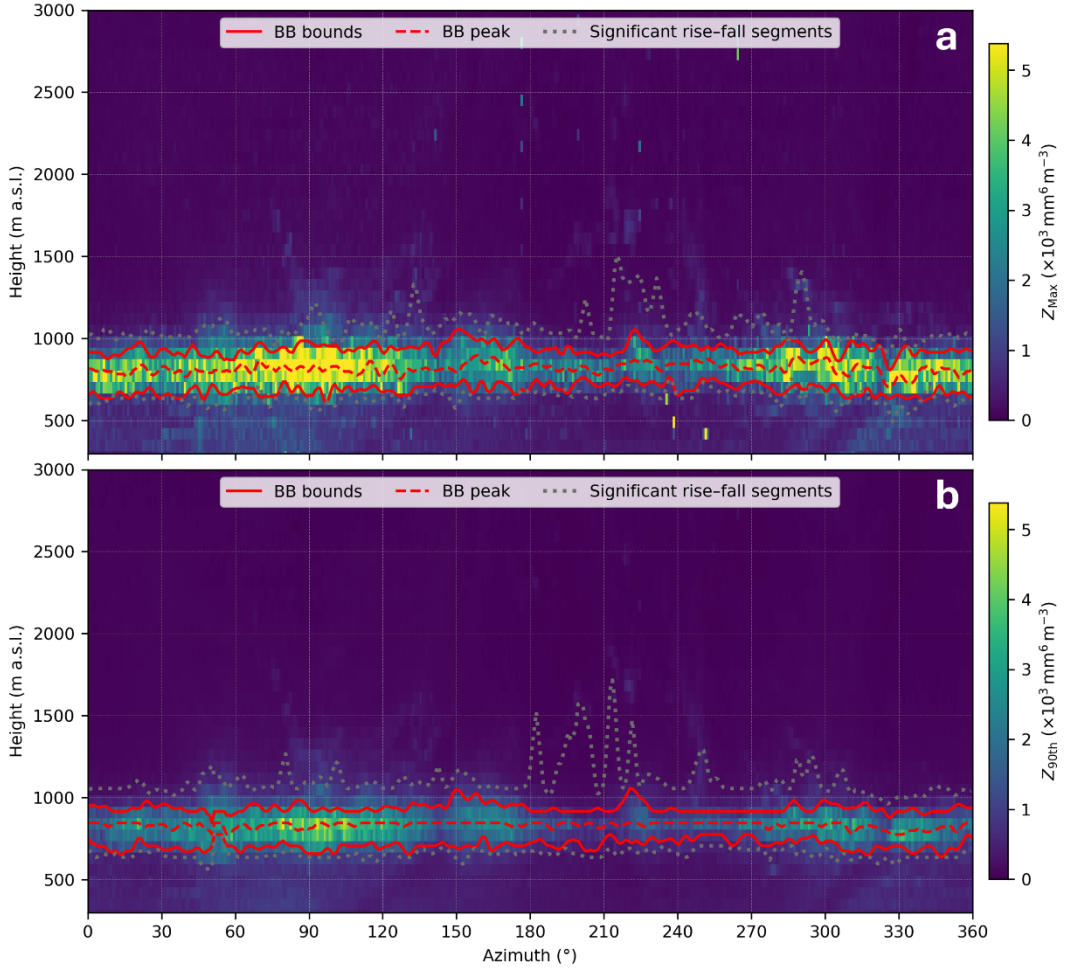

Figure 5: BB detection based on the radial profiles maximum (a) and 90th percentile (b) for the Ängelholm CWR at a 5-min step (namely, 14:00 UTC) on 4 February 2022.

https://doi.org/10.5194/egusphere-2026-7174
Preprint. Discussion started: 24 November 2026
© Author(s) 2026. CC BY 4.0 License.

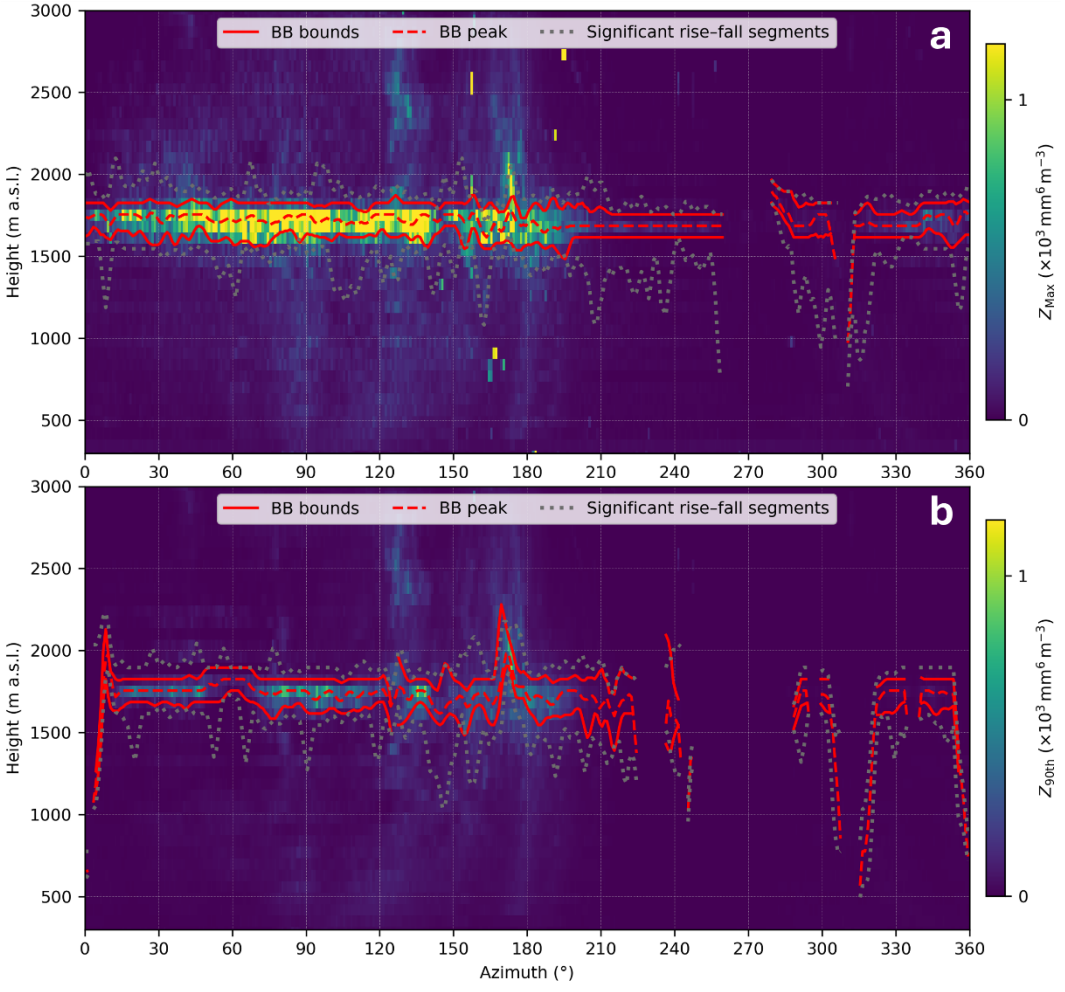

Figure 6: Same as Figure 5, but for a 5-min step (namely, 11:50 UTC) on 18 May 2025.

3.3 Ängelholm CWR-based BB detection using CFAD-based profiles

In this method, the representative profiles are envelope, mode, and median profiles, which are found based on the CFADs constructed in two ways, using absolute frequency and relative frequency.

Figure 7 shows examples from two events. Comparing the CFADs clearly indicates two completely different types of events, where the event from 4 February 2022 (Figure 7a and b) has heavier precipitation with its mode well above 0 dBZ, and the event from 18 May 2025 (Figure 7c and d) is lighter with more diverse distribution of scatterers. Notably, the two types of CFADs based on the absolute frequency (Figure 7a and c) and relative frequency (Figure 7b and d) are generally similar and the applied respective threshold (50 counts vs. the fraction 0.0005) are comparable.

https://doi.org/10.5194/egusphere-2026-7174
Preprint. Discussion started: 24 November 2026
© Author(s) 2026. CC BY 4.0 License.

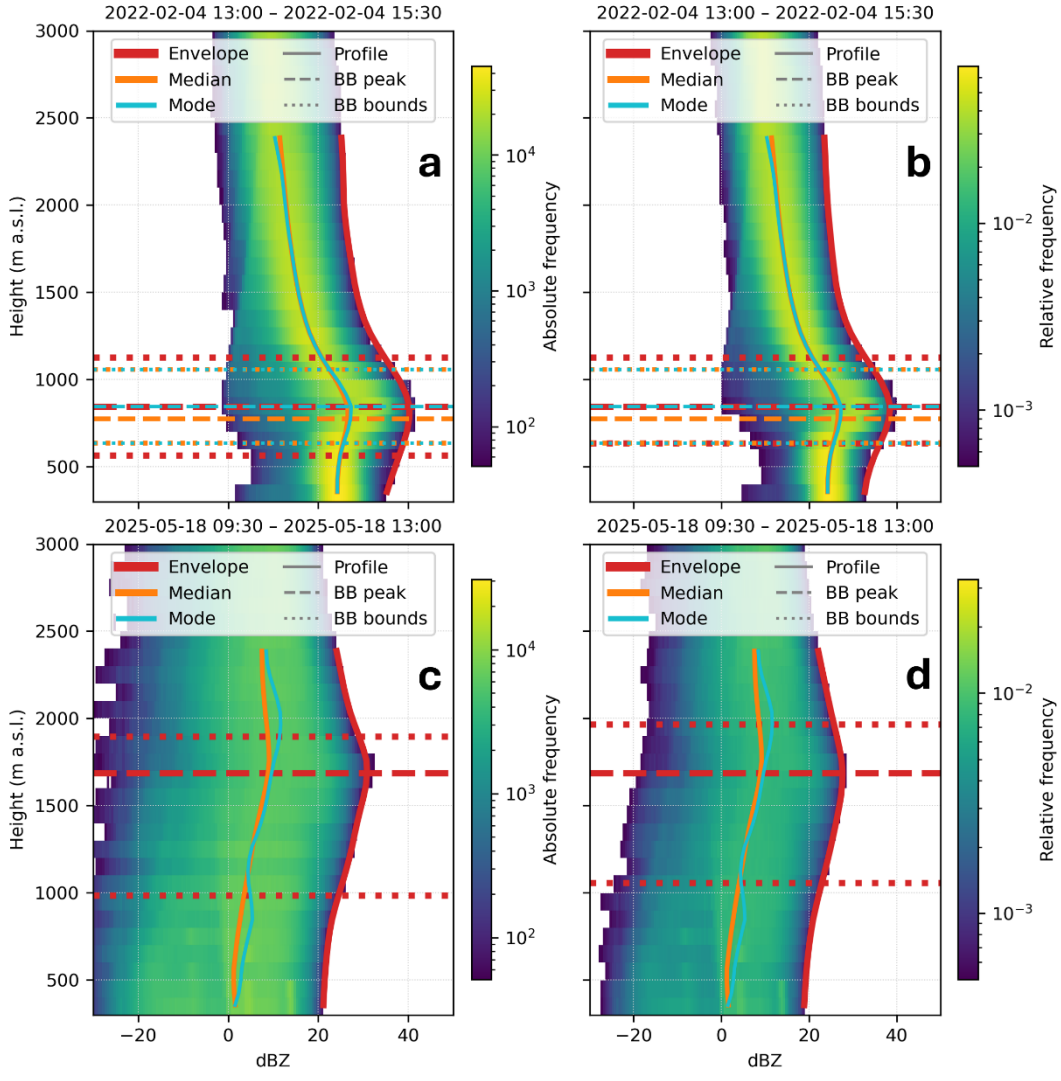

Figure 7: CFAD-based BB detection from the Ängelholm CWR using absolute frequency (a,c) and relative frequency (b,d) for the events on 4 February 2022 (a,b) and 18 May 2025 (c,d). For the latter, there were no valid BB detection based on Median and Mode profiles.

The winter event (Figure 7a and b) has similar results from all three profiles (Envelope, Median, and Mode) defining the BB peak around 800 m a.s.l. and the thickness around 500 m, slightly smaller for relative frequency vs. absolute frequency. In comparison with the MRR observation (Figure 4a), the peak is underestimated by 200 m, and the thickness is more than doubled. The results are comparable with the radial profiles (Figure 5), except for the overestimated BB thickness.

For the event from 18 May 2025 (Figure 7c and d) only the envelope profile produces a well-defined BB. One can argue that the median profile could produce a similar result for the BB peak around 1750 m a.s.l., but this is not shown in the figure because its bounds, together with the mode profile, failed the consistency check. The color bar indicates that the most frequent

https://doi.org/10.5194/egusphere-2026-7174
Preprint. Discussion started: 24 November 2026
© Author(s) 2026. CC BY 4.0 License.

intensity is somewhere outside the plotted range, possibly caused by ground clutter. Contrary to the previous event, the height of BB peak is overestimated by a few hundred meters compared with the MRR-derived height (Figure 4b), but the BB thicknesses is again multiplied.

These two events indicate that CFADs created from data aggregated over the radar domain and time tend to smooth the BB signature and broaden its apparent vertical extent (thicknesses). This interpretation is consistent with the general smoothing effect of profile-aggregation approaches used in melting-layer studies (Sanchez-Rivas and Rico-Ramirez, 2021). These results suggest greater reliance on the BB peak than on the BB bounds when using the CFAD-based methods.

3.4 Comparing event-mean BB heights from MRR and CWR

3.4.1 Radial profiles

Figure 8 illustrates four hexbin plots to compare event-mean BB bottom heights derived from MRR (given N_v=20 and c=3) and CWR-based radial profiles (in four ways). Two panels show height estimates of BBB_{Max}, and BBB_{90th} only from the radial toward the MRR location, whereas the two others exhibit average of BBB_{Max}, and BBB_{90th} height estimates obtained from all radials.

N=302 shown in the title of all panels denotes the number of events with valid BB height estimates from both MRR and CWR. Out of 328 MRR-derived events (Table 3), 26 were excluded due to missing or invalid CWR information. Of these, 16 corresponded to periods when the Ängelholm CWR was not operational (e.g., maintenance or temporary malfunction). The remaining 10 cases had CWR data available but lacked valid BB detection, either along the radial toward the MRR or across all radials.

Each panel also includes the evaluation metrics PCC, SCC, MAE, and PBIAS, allowing visual and quantitative assessment of consistency between the two instruments. All hexbin plots show a generally good agreement between MRR and CWR estimates, with higher frequency of the data points near the x=y line.

The best agreement is obtained for CWR estimations based on the radial toward the MRR, with a PCC=SCC=0.88, MAE=169 m, and PBIAS=-4.3% for BBB_{Max}, e.g., compared with the corresponding metrics (0.85, 186 m, and -5.6%) obtained based on the average across all radials.

The poorest performance according to most metrics is observed for the average BBB_{90th} heights across all radials, with PCC=0.77, SCC=0.76, MAE=220 m, and PBIAS=-4.3%. When only the radial toward the MRR was considered, BBB_{90th} estimates showed performance comparable to BBB_{Max}, with PCC=SCC=0.87, MAE=171 m, and PBIAS=-1.4%.

https://doi.org/10.5194/egusphere-2026-7174
Preprint. Discussion started: 24 November 2026
© Author(s) 2026. CC BY 4.0 License.

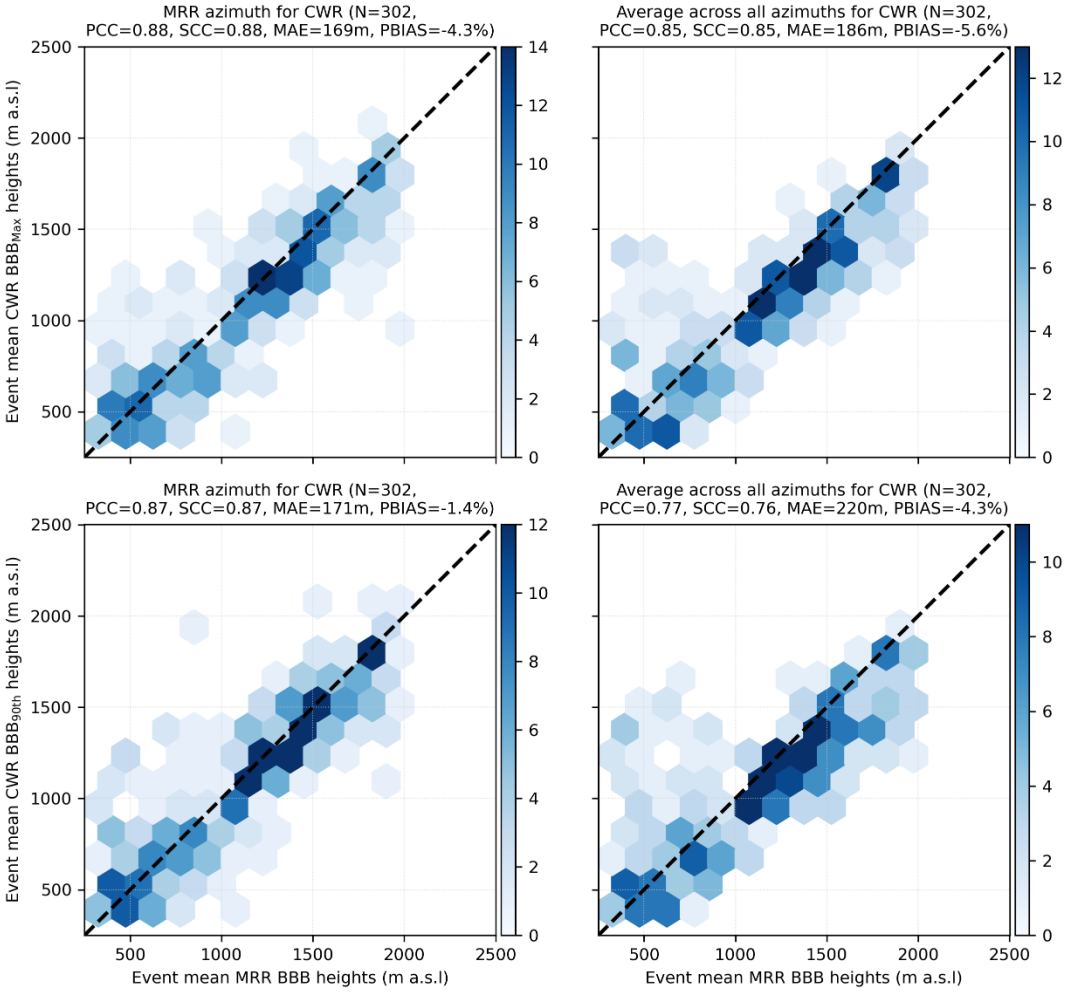

505 **Figure 8: Hexbin plots comparing event-mean bright-band bottom (BBB) heights derived from MRR and CWR observations. CWR-based estimates are based on the maximum profiles (upper row) and the 90th percentile profiles (lower row). Results are shown for estimates along the radial toward the MRR (left column) and for averaged BB bottom heights across all available CWR radials (right column). Color intensity represents the number of data points within each hexagonal bin.**

510 CWR estimates of the BB peak and top heights also show better performance when based on the radial toward the MRR than when averaged across all radials (see Figure 9 and Figure 10).

For BB peak (Figure 9), the best PCC (0.86), SCC (0.87), MAE (172 m), and PBIAS (-1.5%) all belong to BBP_{Max} estimated from the radial toward the MRR. Note that, the three additional data points for the BB peak compared with the BB bottom and top (i.e., N=305 vs. 302) result from three BB peaks that fell outside the bounds derived from the gradient extrema but were 515 confirmed using the significant rise–fall segmentation method.

https://doi.org/10.5194/egusphere-2026-7174
Preprint. Discussion started: 24 November 2026
© Author(s) 2026. CC BY 4.0 License.

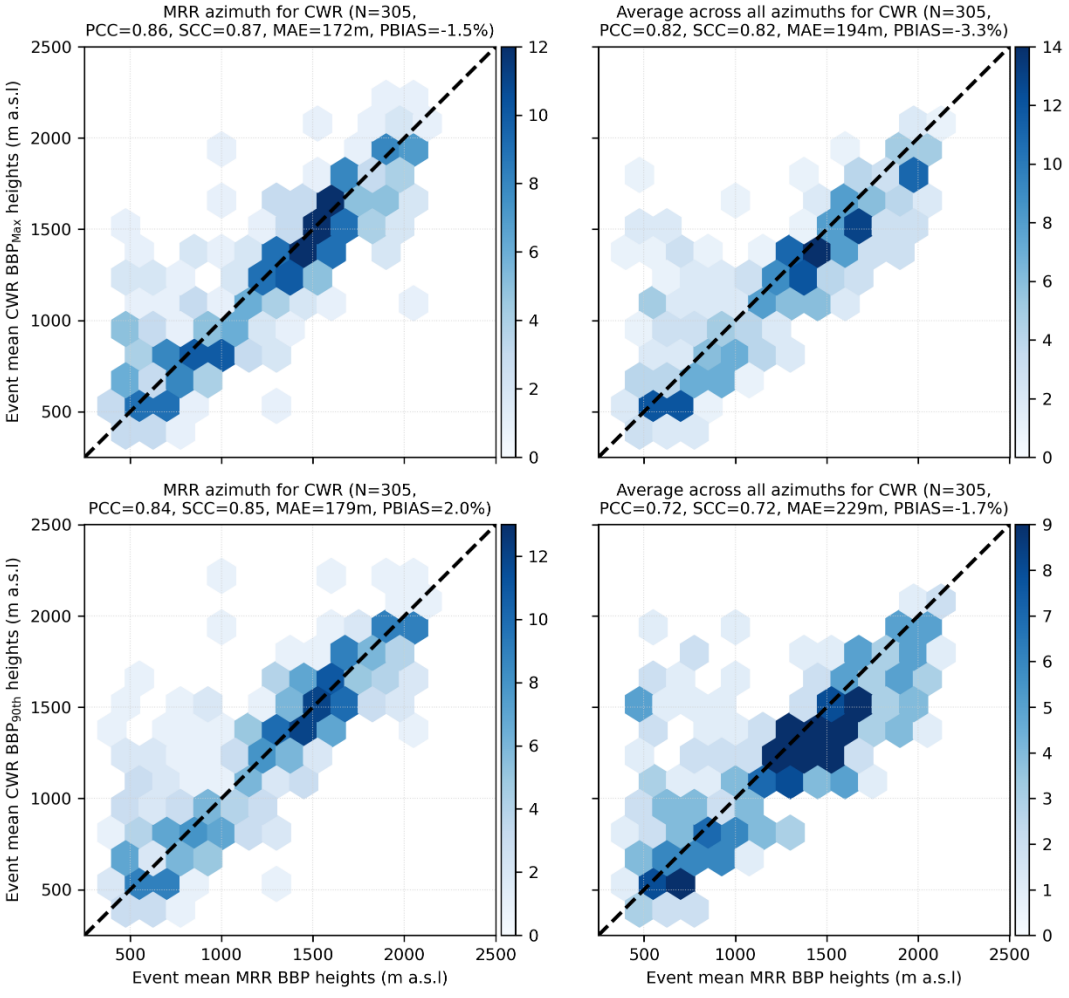

Figure 9: Same as Figure 8, but for bright-band peak (BBP) heights.

For BB top (Figure 10), the best correlation (PCC=SCC=0.88) and MAE (163 m) are achieved for BBT_{Max}, while the best PBIAS (1.3%) is again observed for BBT_{90th}, using only the radial toward the MRR.

The consistently better performance of estimates based on the radial toward the MRR further supports the use of radial profiles, as averaging across radials tends to smooth the BB signature and reduce its local representativeness, consistent with the general smoothing effect of spatial profile aggregation discussed earlier for the CFAD-based methods (Sanchez-Rivas and Rico-Ramirez, 2021). However, it should be noted that averaging BB heights derived from individual radial profiles is fundamentally different from estimating BB heights directly from aggregated CFADs.

https://doi.org/10.5194/egusphere-2026-7174
Preprint. Discussion started: 24 November 2026
© Author(s) 2026. CC BY 4.0 License.

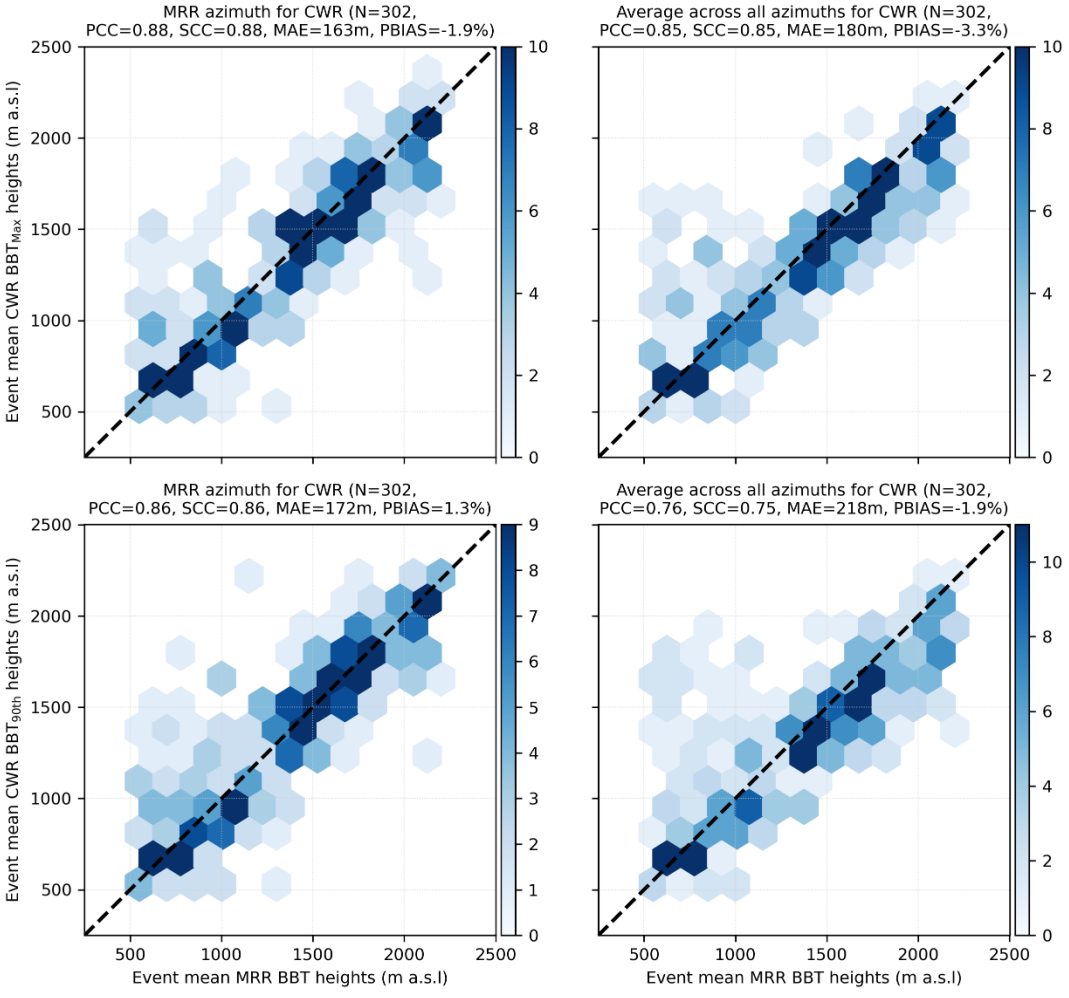

Figure 10: Same as Figure 8, but for bright-band top (BBT) heights.

3.4.2 CFAD-based profiles

This section presents results of the hexbin plots and evaluation metrics to compare event-mean MRR reference BB heights with CWR-derived estimates obtained from six CFAD-based methods: envelope, mode, and median, each applied with count and fraction thresholds based on absolute- and relative-frequency CFADs, respectively. The results are presented in six panels of Figure 11, Figure 12, and Figure 13 for BB bottom, BB peak, and BB top, respectively. The panels are arranged with absolute and relative frequency methods in the columns, and envelope, mode, and median methods in the rows.

The three profiles correspond differently to the MRR depending on the BB characteristics. BB bottom is best represented by the median profile based on the absolute frequency, but still the PCC is below 0.5 and the MAE is greater than 300 m (Figure 11).

https://doi.org/10.5194/egusphere-2026-7174
Preprint. Discussion started: 24 November 2026
© Author(s) 2026. CC BY 4.0 License.

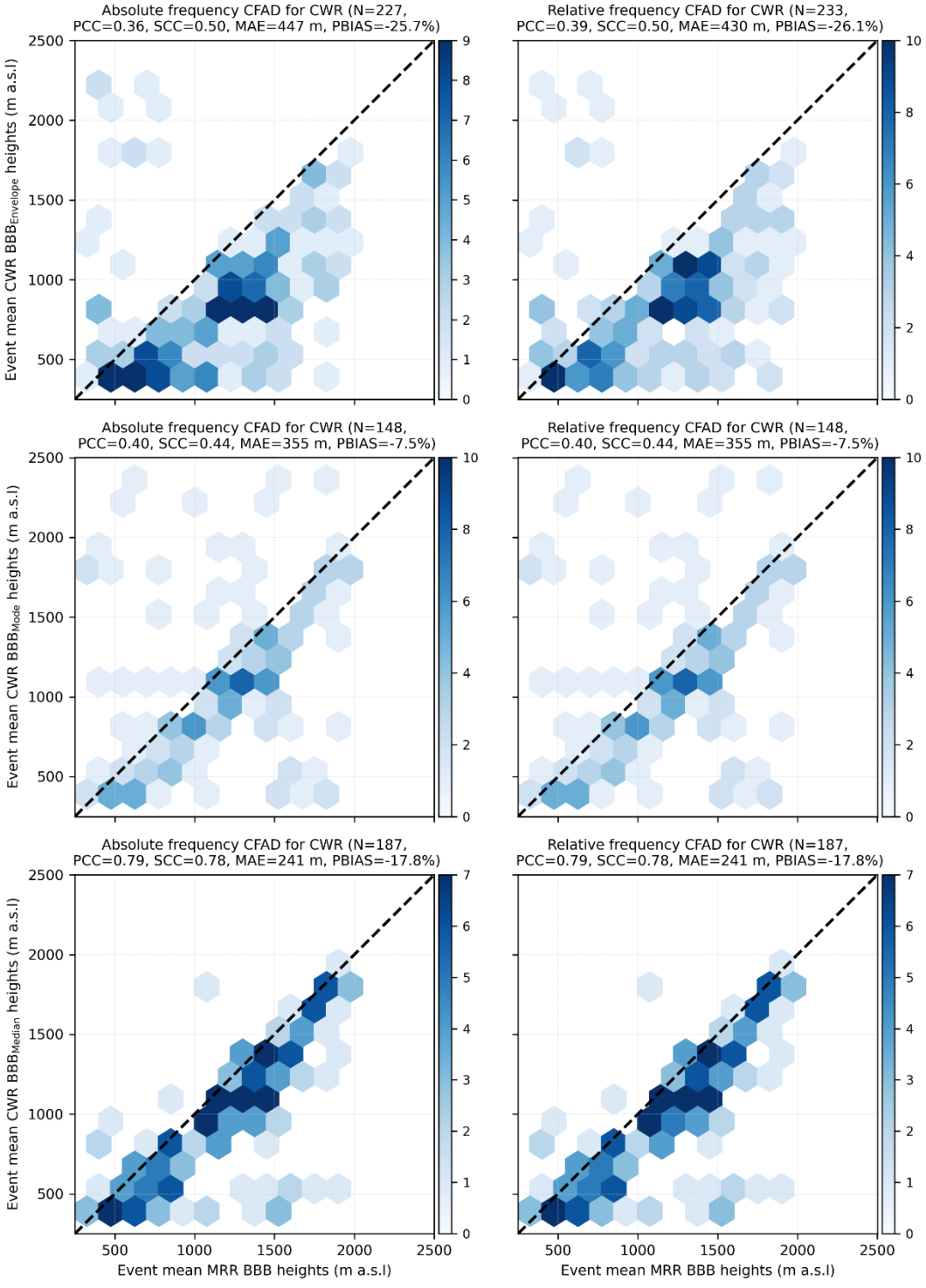

Figure 11: Hexbin plots comparing event-mean MRR bright-band bottom (BBB) heights with CWR-derived estimates for the six CFAD-based extraction methods. Rows show the reflectivity metrics (envelope, mode, and median), and columns show the absolute- and relative-frequency methods. Color intensity represents the number of data points within each hexagonal bin.

https://doi.org/10.5194/egusphere-2026-7174
Preprint. Discussion started: 24 November 2026
© Author(s) 2026. CC BY 4.0 License.

It is worth noting that the envelope is the worst of these three to define the BB bottom (Figure 11), which may partly be associated with the higher number of the BB events identified using envelope (227 and 233) than mode (148) and median (187). For BB peak (Figure 12), the envelope profile from the relative frequency represents the MRR observations best with PCC=0.71 and MAE=222 m, although the PCC for the envelope profile from the absolute frequency is slightly higher. Figure 13 indicates again that the envelope from the relative fraction best represents the BB top.

Conceptually, the envelope profile within the CFAD framework is closely related to the maximum-reflectivity radial profile used in this study, as both retain the highest reflectivity values associated with the BB. However, the envelope profile is derived after aggregating radar observations over all radials and the entire event, whereas the radial profile preserves the reflectivity structure within an individual radial and time step. This difference likely explains why the envelope generally performed best among the CFAD-based representations, while still being outperformed by the maximum-reflectivity radial profiles presented earlier.

In general, the height differences may be explained by the standard atmosphere assumptions used for the beam propagation height calculation in the CFAD-based methods, while anomalous propagation can occur frequently depending on actual atmospheric conditions (Norin, 2023).

Notably, the Ängelholm CWR has a known issue within an approximately 30° azimuthal sector toward north, due to partial beam blockage from tall trees in short ranges. As exemplified in the study of Petersson Wårdh et al. (2026), this can cause significant underestimation of precipitation in the affected sector, especially from the lowest elevation angles. The issue may therefore affect the accuracy of the BB height estimates based on the full radar volume data.

The lower number of valid cases (N) for the CFAD-based methods compared with the radial-profile methods is consistent with the previously discussed lower capability of the former to detect BB bounds. Therefore, if the objective is to derive representative average BB heights for a weather radar over a given period, averaging BB heights estimated from individual radial profiles and time steps is likely to be more reliable than estimating BB heights directly from aggregated CFAD profiles.

Overall, the better agreement of the radial-profile methods with the MRR observations suggests that BB detection benefits from preserving the spatial and temporal variability of the radar measurements. In the present study, BB heights were first estimated independently from each radial profile and then averaged when needed, whereas the CFAD-based methods estimated BB heights after aggregation of reflectivity over all radials and the entire event. The latter approach smooths the reflectivity structure defining the BB, reducing the sharpness of the gradient extrema and broadening the apparent BB thickness, which likely contributes to the lower agreement with the MRR observations.

Part of the remaining discrepancy is also expected from the fundamentally different sampling geometries of the two instruments, with the vertically pointing MRR providing high-resolution measurements within a single atmospheric column, whereas the volume-scanning CWR samples progressively larger volumes at increasing range.

https://doi.org/10.5194/egusphere-2026-7174
Preprint. Discussion started: 24 November 2026
© Author(s) 2026. CC BY 4.0 License.

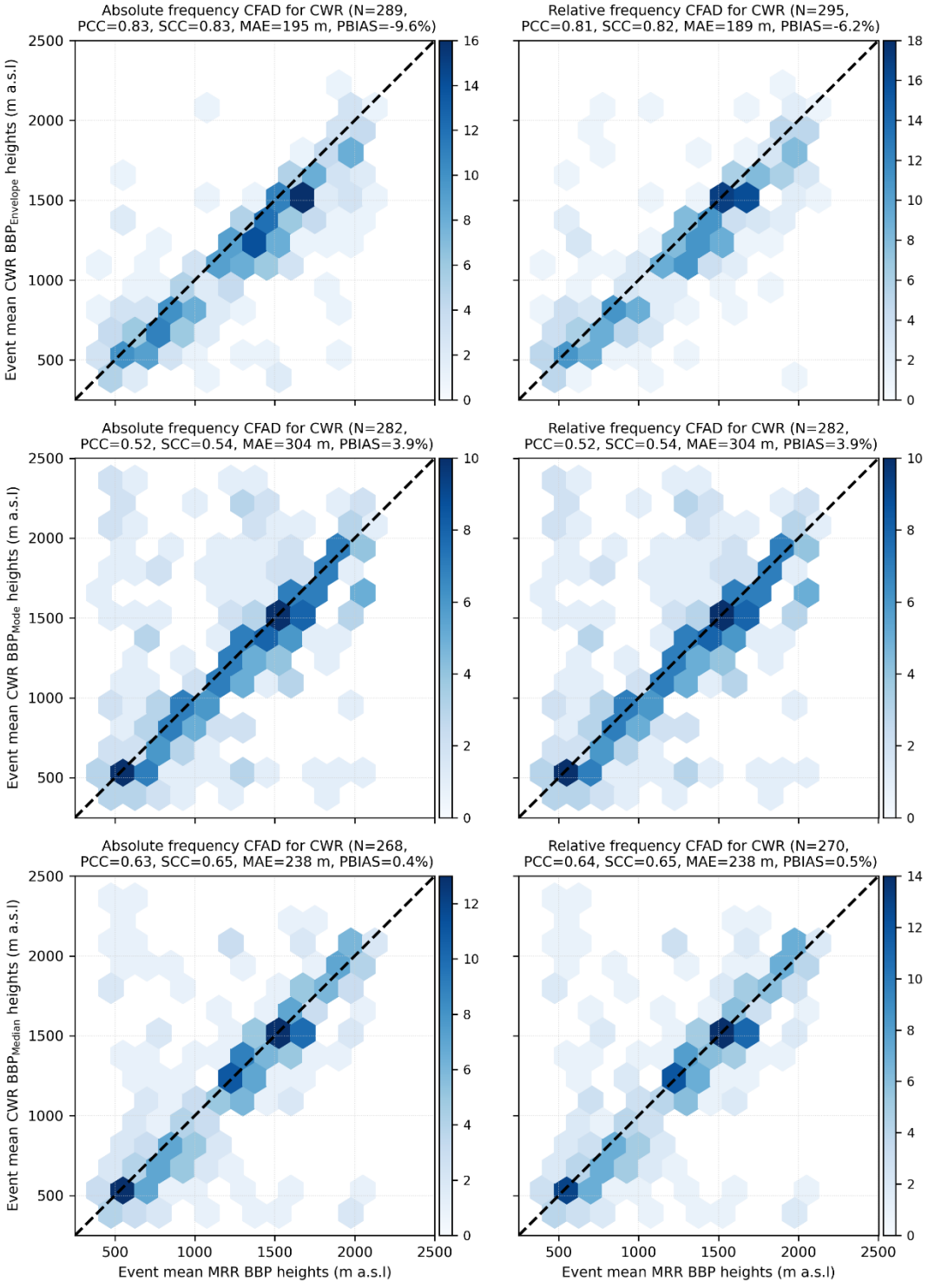

575 **Figure 12: Same as Figure 11, but for bright-band peak (BBP) heights.**

https://doi.org/10.5194/egusphere-2026-7174
Preprint. Discussion started: 24 November 2026
© Author(s) 2026. CC BY 4.0 License.

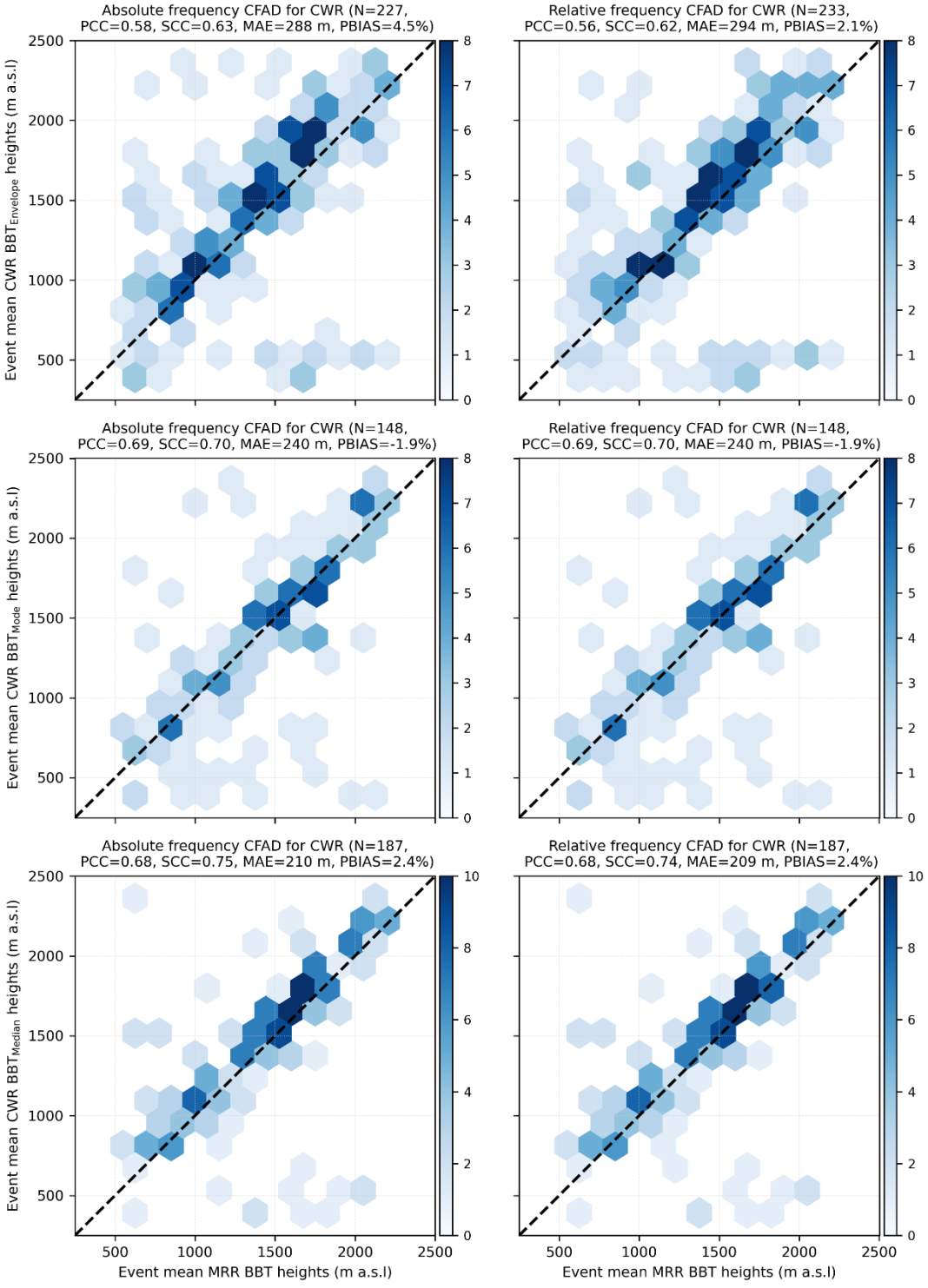

Figure 13: Same as Figure 11, but for bright-band top (BBT) heights.

https://doi.org/10.5194/egusphere-2026-7174
Preprint. Discussion started: 24 November 2026
© Author(s) 2026. CC BY 4.0 License.

3.5 Seasonal probability distribution for 5-min widespread stratiform samples

In addition to the event-mean comparisons, seasonal BB-height distributions were evaluated to assess whether the CWR-based method reproduces the seasonal variability observed by the MRR. As described in Sect. 2.7, the analysis was restricted to widespread stratiform samples. Because the maximum-reflectivity radial-profile method showed the best overall performance in the event-mean analyses, only this method was considered here.

Figure 14 shows the seasonal distributions of BB bottom height based on the 5-min CWR–MRR observations that were classified as widespread stratiform using the radial profile method.

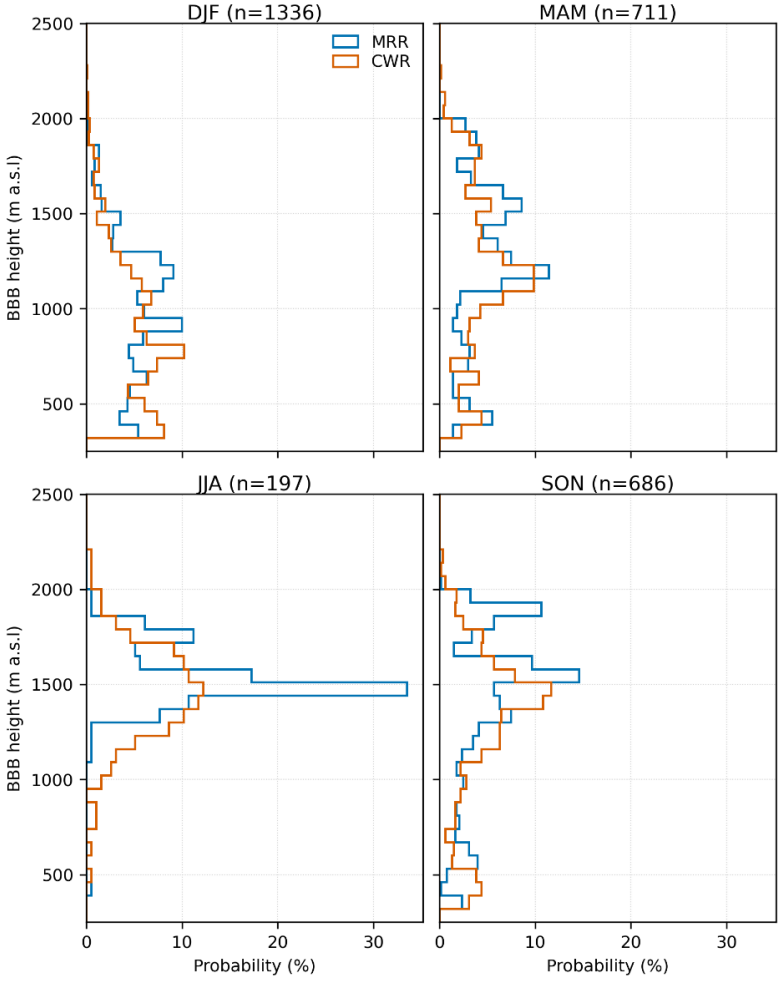

Figure 14: Seasonal distribution of bright-band bottom (BBB) height under widespread stratiform condition. Histograms show the probability density for the three-month seasons DJF, MAM, JJA, and SON (n denotes the number of matched 5-min CWR–MRR observations).

https://doi.org/10.5194/egusphere-2026-7174
Preprint. Discussion started: 24 November 2026
© Author(s) 2026. CC BY 4.0 License.

It reveals a clear difference in variations across seasons. Lower BB bottom height occurs predominantly in winter (DJF), where most values are below 1250 m a.s.l., with a rather uniform distribution. In summer (JJA) and autumn (SON), however, they are predominantly peaking around 1500 m a.s.l., while the most frequent values are around 1200 m a.s.l in spring (MAM). Overall, the distributions derived from CWR and MRR show similar shapes and modal heights, indicating good consistency. Figure 15 and Figure 16 show similar seasonal variations in the distributions and overall agreement between CWR–MRR distributions for BB peak and BB top, respectively. The reason for higher numbers of time steps used in these two BB features compared with BB bottom is their higher spatial homogeneity and coherence across radials due to lower susceptibility to ground clutter errors. The over- and under-estimations of all BB characteristic heights relative to the MRR-derived reference estimates may be related to differences in sampling geometry and retrieval methodology. Also, the relatively small number of observations in JJA (197−217) may explain the noisier distribution compared with the other seasons.

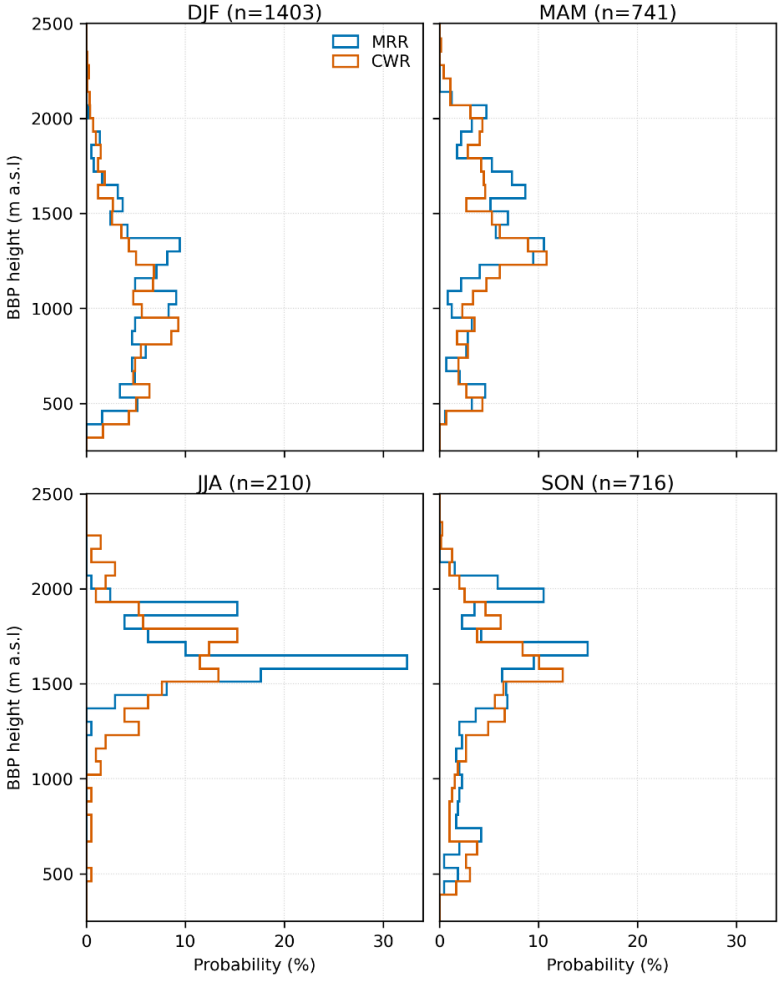

Figure 15: Same as Figure 14, but for bright-band peak (BBP) height.

https://doi.org/10.5194/egusphere-2026-7174
Preprint. Discussion started: 24 November 2026
© Author(s) 2026. CC BY 4.0 License.

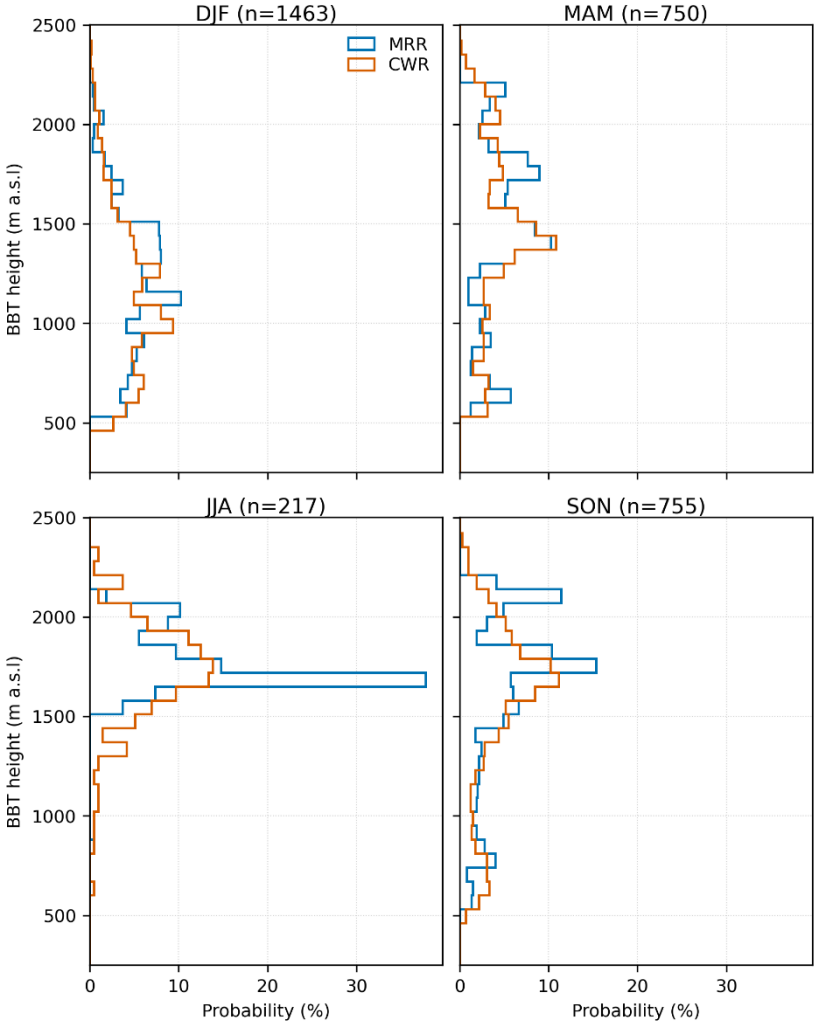

Figure 16: Same as Figure 14, but for bright-band top (BBT) height.

Table 4 summarizes the evaluation metrics for the CWR–MRR comparison. Correlations are high for all BB levels (PCC and SCC ≈ 0.85–0.87), and the mean absolute error ranges from about 174 to 183 m. Negative PBIAS values (−3.8% to −7.4%) indicate that CWR estimates are slightly lower than those from MRR on average, with the largest bias for the BB bottom height. These negative biases may partly reflect uncertainties in radar-beam height estimation associated with the straight-line propagation assumption, as well as differences in sampling geometry and retrieval methodology between the CWR and MRR. The slightly lower correlations and higher errors, compared with the event-mean BB heights obtained from radial profiles (Sect. 3.4.1), are associated with higher variability in the 5-min data relative to the event-mean values.

https://doi.org/10.5194/egusphere-2026-7174
Preprint. Discussion started: 24 November 2026
© Author(s) 2026. CC BY 4.0 License.

Table 4. Evaluation metrics for CWR-derived bright-band (BB) characteristic heights relative to the MRR-derived reference BB heights for all matched 5-min widespread stratiform samples.

BB feature	N	PCC	SCC	MAE (m)	PBIAS (%)
BB bottom	2930	0.85	0.87	182.6	-7.4
BB peak	3070	0.85	0.86	178.4	-4.7
BB top	3185	0.86	0.86	174.2	-3.8

Nevertheless, the good agreement between the seasonal CWR and MRR distributions, together with the accurate event-mean BB-height estimates presented in Sect. 3.4.1, indicates that the proposed radial approach captures both the seasonal and event-scale variability of the melting layer observed by the MRR, supporting its potential for operational bright-band detection from volume-scanning weather radars.

These generally promising results should also be considered in light of resonance scattering effect, which may be more pronounced for melting particles at C-band than for radars operating at longer wavelength (e.g., S-band; Fabry and Szyrmer, 1999; Zhu et al., 2025). Shorter radar wavelengths, such as X-band, may conversely exhibit different sensitivities to DSD. Therefore, the performance of the proposed method may differ for radars operating at other wavelengths and should be evaluated separately.

Nevertheless, the homogeneity checks of BB detections across radials used here provide a useful basis for precipitation-type classification (stratiform versus convective) using operational WRs, without relying on supplementary observations that have also been used for this purpose (Hosseini et al., 2025).

To avoid errors in the BB bottom estimates, the separation between the BB peak and bottom heights may be estimated from the separation between the BB peak and top heights. Specialized models can be trained using the MRR observations from temporary installations as suggested previously (Hosseini et al., 2025, 2023) to represent the expected thickness for the prevailing climates of each operational radar.

The radial approach presented here was tested for one operational WR in Sweden, but it can be evaluated for additional WRs under different climatic and environmental conditions once further reference data, for example from new radar profilers or WR birdbath scans, become available. In addition, the approach was developed using only horizontally polarized reflectivity and can be compared with operational methods based on polarimetric WR observations (Sanchez-Rivas and Rico-Ramirez, 2021) when dual-polarization operation becomes available.

3.6 Rainfall estimation bias relative to the bright-band

To evaluate the impact of BB on QPE, the bias of CWR-derived rainfall estimates from different elevation angles relative to rain-gauge observations were calculated, as described in Sect. 2.8. Although the gauges are located at different CWR azimuths and ranges, the stratiform precipitation events considered here allow the sampled vertical reflectivity profiles to be assumed representative.

https://doi.org/10.5194/egusphere-2026-7174
Preprint. Discussion started: 24 November 2026
© Author(s) 2026. CC BY 4.0 License.

Accordingly, the CWR QPE from different elevation angles is compared with 15-min rainfall observations from the three rain-gauge stations, using the radar bin closest to each gauge. The BB heights were averaged over the corresponding 15-min time steps. Figure 17a and b show the absolute and relative radar rainfall-estimation bias relative to the rain gauges as a function of vertical distance from the BB. The detected BB heights vary over time throughout the 2021–2025 period, but in this figure the observations are aligned relative to their corresponding BB boundaries, so the BB is shown artificially as a fixed vertical interval. The vertical axis therefore represents the vertical distance between the center of each radar sampling bin and the closest BB boundary (bottom or top, depending on whether the bin is below or above the BB). Thus, the scatter represents observations from different times, locations, and elevation angles at different vertical distances from the BB.

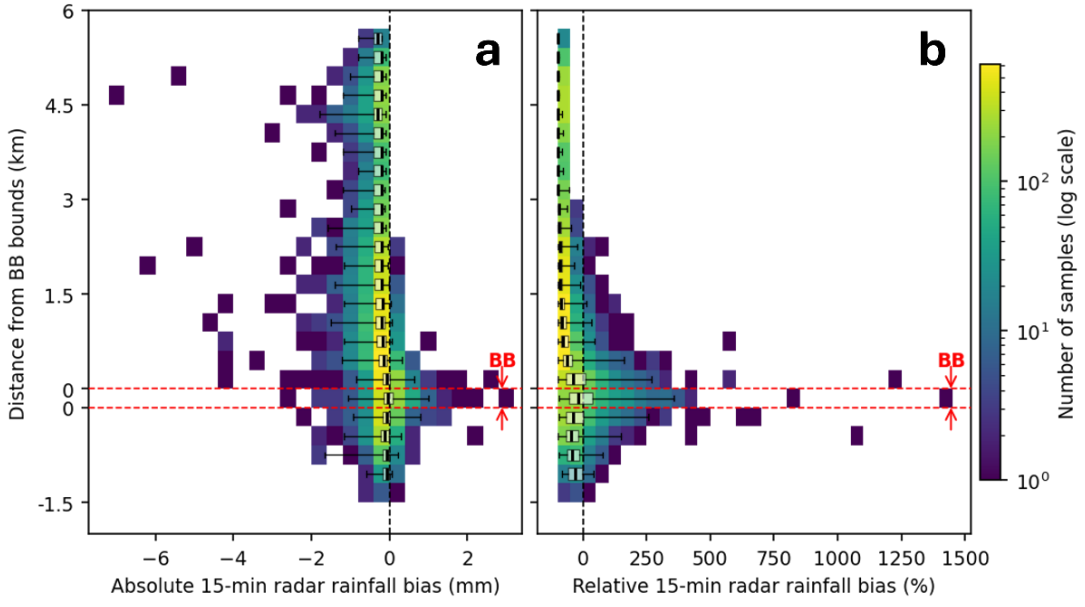

Figure 17: Ängelholm C-band weather radar 15-min rainfall-estimation bias relative to observations from the rain gauges as a function of the vertical distance between the radar-beam center and the nearest bright-band (BB) boundary, represented as absolute bias in mm (a) and relative bias in percent (b). Horizontal boxplots summarize the bias distribution within each distance interval (300 m) and within the BB interval, which is shown artificially between the two horizontal dashed lines. The box edges indicate the 25th and 75th percentiles, the line within each box indicates the median, and the whiskers extend to the 1st and 99th percentiles.

Measurements start from approximately 2 km below the BB and are truncated at 6 km above it for illustration. Notably, positive biases are largely confined to the BB and its immediate vicinity. In contrast, negative biases dominate across most sampling heights and become increasingly pronounced with increasing distance from the BB, particularly above it, where the underestimation is accompanied by greater variability. This behavior is consistent with the lower dielectric factor of snow compared with rain, together with additional effects such as beam overshooting, evaporation, and hydrometeor advection before precipitation reaches the ground. Below the BB, these effects are minimized, resulting in a relatively small median bias

https://doi.org/10.5194/egusphere-2026-7174
Preprint. Discussion started: 24 November 2026
© Author(s) 2026. CC BY 4.0 License.

and low variability, although overestimations are also observed, particularly immediately beneath the BB. The overestimations near the BB can be explained by the fact that the radar beamwidth can exceed the thickness of the BB and therefore partly samples it. Within the BB, the frequencies of under- and overestimation are more balanced, resulting in a median bias close to zero, although the spread of the bias distribution increases substantially.

It should also be noted that the radar rainfall estimates used here were derived without systematic bias correction or path-integrated attenuation correction. Applying such corrections would generally be expected to shift the bias distributions towards more positive values, potentially resulting in greater overestimation within the BB and reduced underestimation at greater distances outside it. Nevertheless, the substantially greater variability of rainfall estimates within and around the BB indicates that BB location remains relevant for the radar-based QPE. This is consistent with operational radar QPE systems, such as the Multi-Radar Multi-Sensor (MRMS) system operational at the U.S. National Centers for Environmental Prediction, where melting-layer detection supports the application of vertical profile of reflectivity (VPR) corrections to reduce BB-related errors (Zhang et al., 2016).

4 Conclusions and outlook

Volume-scanning C-band weather-radar reflectivity data were used to detect BB characteristic heights (bottom, peak, and top) relative to MRR-derived reference melting-layer events within the MRR observational height range. Among the evaluated approaches, azimuthal (radial) reflectivity profiles outperformed event-based CFAD-derived profiles, providing the strongest agreement with the reference event-mean BB heights and reproducing the seasonal distributions of 5-min BB heights under widespread stratiform conditions.

The variability of BB-height estimates across radials proved useful as an indicator of spatial coherence. A simple homogeneity criterion based on the number of valid radial detections and their coefficient of variation effectively identified widespread stratiform conditions while filtering situations with less coherent BB structure. Because these criteria rely solely on information available from individual radar volumes, they are well suited for operational implementation.

Operational implementations may adopt stricter spatial or temporal homogeneity criteria depending on the intended application. For example, higher thresholds for the number of valid radials or additional temporal consistency checks could be introduced to further improve the robustness of BB detection. Applying the homogeneity assessment to contiguous azimuthal sectors rather than the full 360° coverage would also allow reliable BB detection within coherent portions of precipitation systems, particularly when other sectors contain convective or non-precipitating regions. While such extensions may improve the robustness of retrospective BB analyses, the spatial homogeneity criterion alone already provided satisfactory results from individual radar volumes, making it well suited for real-time operational applications.

Although CFAD-based methods provide a complementary domain-wide description of the vertical reflectivity structure, they performed less accurately than the azimuthal profile methods because aggregation across radials and time tends to smooth the

https://doi.org/10.5194/egusphere-2026-7174
Preprint. Discussion started: 24 November 2026
© Author(s) 2026. CC BY 4.0 License.

BB signature. Nevertheless, both approaches are conceptually related and could be combined in future studies to exploit their complementary strengths.

The proposed methodology is expected to be applicable to other weather-radar systems, although differences in radar wavelength, beam geometry, and local sources of beam blockage should be considered. However, the performance of the radial BB detection approach at radar ranges beyond those evaluated in this study requires further investigation because the native sampling volumes from the available elevation angles become larger and more vertically sparse with increasing distance from the radar.

The presented methodology provides a practical basis for an operational melting-layer product derived from volumetric weather-radar observations. Such a product could support radar quantitative precipitation estimation through improved VPR corrections, attenuation correction strategies, and the application of precipitation-phase-dependent reflectivity–rainfall relationships. Beyond QPE, melting-layer information could also support the evaluation of numerical weather prediction microphysics and the assimilation of atmospheric thermodynamic and hydrometeor profiles. In multi-radar networks, where radar compositing or merging is applied, the spatial variability of BB-height estimates within overlapping coverage areas could additionally be used as an indicator of uncertainty for weighting or ranking the corresponding radar reflectivity observations.

https://doi.org/10.5194/egusphere-2026-7174
Preprint. Discussion started: 24 November 2026
© Author(s) 2026. CC BY 4.0 License.

Appendix A

The radial profiles per given radial of the Ängelholm CWR are constructed using the maximum and 90th percentile of the 28–43 reflectivity data collected at each height bin according to Table A1.

Table A1– Number of scanning weather radar range gates assigned to each MRR-aligned 70-m height bin for the Ängelholm CWR. Counts are based on beam-center heights which are computed for straight-line propagation at each elevation angle (θ), considering a spherical Earth. The last column shows the number of contributing gates summed over all elevation angles.

Height bin (±35 m)	θ=0.5°	θ=1°	θ=1.5°	θ=2°	θ=2.5°	θ=4°	θ=8°	θ=14°	θ=24°	θ=40°	Sum
356	12	7	5	4	6	4	2	2	0	1	43
426	12	8	5	4	6	4	2	1	1	0	43
496	11	7	5	4	7	4	2	1	1	1	43
566	10	7	5	3	6	4	2	1	0	0	38
636	10	6	5	4	6	4	2	1	1	0	39
706	9	7	5	4	6	4	2	1	1	1	40
776	9	6	5	4	6	4	2	1	0	0	37
846	8	6	4	3	7	4	2	2	1	1	38
916	8	7	5	4	6	4	2	1	1	0	38
986	8	6	5	4	6	3	2	1	0	1	36
1056	8	5	4	3	6	4	2	1	1	0	34
1126	7	6	5	4	6	4	2	1	1	0	36
1196	7	6	4	4	6	4	2	1	1	1	36
1266	7	5	5	3	6	4	2	2	0	0	34
1336	7	6	4	4	5	4	2	1	1	1	35
1406	6	5	4	3	6	4	2	1	1	0	32
1476	7	5	4	4	6	4	2	1	0	1	34
1546	6	6	5	3	6	4	2	1	1	0	34
1616	6	5	4	4	6	3	2	1	1	0	32
1686	6	5	4	3	5	4	2	1	0	1	31
1756	6	5	4	3	6	4	2	2	1	0	33
1826	6	5	4	4	6	4	2	1	1	1	34
1896	6	5	4	3	6	4	2	1	0	0	31
1966	5	4	4	3	5	3	2	1	1	1	29
2036	6	5	4	4	6	4	2	1	1	0	33
2106	5	5	4	3	5	4	2	1	0	1	30
2176	6	4	4	3	6	4	2	2	1	0	32
2246	5	5	4	4	6	4	2	1	1	0	32
2316	5	4	3	3	5	3	2	1	1	1	28
2386	5	5	4	3	6	4	2	1	0	0	30
Sum	219	168	131	106	177	116	60	35	20	13	1045 (total)

https://doi.org/10.5194/egusphere-2026-7174
Preprint. Discussion started: 24 November 2026
© Author(s) 2026. CC BY 4.0 License.

Code and data availability

The Python implementation of the core contributions of the study on radial bright-band detection, together with example data and instructions for reproducing Figs. 5 and 6, is available at https://github.com/hasan-hosseini/radial-bright-band. Version 1.0.3 of the repository, prepared for this manuscript, is permanently archived on Zenodo (Hosseini, 2026).

Author contributions

According to the CRediT Taxonomy: Conceptualization (idea by Hasan H, formulation and evolution of aims by Hasan H & Hossein H, with help of all authors during the process), Project administration (Hasan H), Data curation, Validation, Visualization, Writing – original draft preparation (Hasan H, with help of DJ who carried out the CFAD-based analysis), Writing – review and editing (substantially by all authors), Funding acquisition (Hasan H, Hossein H, JO, RB, HK, DJ, and RvB), Formal analysis, Investigation, Methodology and Software (Hasan H, with help of DJ in the CFAD-based analysis, and RvB in the radar-gauge bias analysis).

Competing interests

The authors declare no competing interests concerning this article.

Acknowledgements

This research was conducted at the SMHI offices in Gothenburg and Norrköping, Sweden, and at Lund University, Lund, Sweden. The authors acknowledge VA Syd for providing data from the Micro Rain Radar (MRR) and its collocated rain gauge, and SMHI for providing data from the C-band weather radar and the additional rain-gauge stations used in this study.

Financial support

This research was funded by the Swedish Research Council for Sustainable Development (Formas) under grant no. 2021-01629 (HyPrecip project). The work was also supported by co-financing from the Swedish Civil Defence and Resilience Agency (MCF) and the Swedish Meteorological and Hydrological Institute (SMHI) through the Paraply project.

Review statement

The review statement will be added by Copernicus Publications listing the handling editor as well as all contributing referees according to their status anonymous or identified.

https://doi.org/10.5194/egusphere-2026-7174
Preprint. Discussion started: 24 November 2026
© Author(s) 2026. CC BY 4.0 License.

References

Atlas, D., Rosenfeld, D., and Wolff, D. B.: Climatologically Tuned Reflectivity–Rain Rate Relations and Links to Area–Time Integrals, Journal of Applied Meteorology (1988-2005), 29, 1120–1135, 1990.

Benarroch, A., Siles, G. A., and Riera, J. M.: Height of the 0°C Isotherm and the Melting Layer in Madrid: Comparison of Estimations from Different Sensors, 2022 16th European Conference on Antennas and Propagation, EuCAP 2022, https://doi.org/10.23919/EUCAP53622.2022.9769329, 2022.

Brast, M. and Markmann, P.: Detecting the melting layer with a micro rain radar using a neural network approach, Atmos. Meas. Tech., 13, 6645–6656, https://doi.org/10.5194/AMT-13-6645-2020, 2020.

Cao, N., Yao, Z., Shu, Z., Chang, Z., Mu, J., Zhu, H., and Lin, T.: Topographic Effects on Stratiform Precipitation Observed by Vertically Pointing Micro Rain Radars at Ridge and Valley Sites in the Liupan Mountains Area, Northwest China, Water (Basel)., 15, 134, https://doi.org/10.3390/w15010134, 2022.

Cha, J. W., Chang, K. H., Yum, S. S., and Choi, Y. J.: Comparison of the bright band characteristics measured by Micro Rain Radar (MRR) at a mountain and a coastal site in South Korea, Adv. Atmos. Sci., 26, 211–221, https://doi.org/10.1007/S00376-009-0211-0, 2009.

Fabry, F. and Szyrmer, W.: Modeling of the Melting Layer. Part II: Electromagnetic, J. Atmos. Sci., 56, 3593–3600, https://doi.org/10.1175/1520-0469(1999)056<3593:MOTMLP>2.0.CO;2, 1999.

Fehlmann, M., Gascón, E., Rohrer, M., Schwarb, M., and Stoffel, M.: Estimating the snowfall limit in alpine and pre-alpine valleys: A local evaluation of operational approaches, Atmos. Res., 204, 136–148, https://doi.org/10.1016/J.ATMOSRES.2018.01.016, 2018.

Field, P. R. and Heymsfield, A. J.: Importance of snow to global precipitation, Geophys. Res. Lett., 42, 9512–9520, https://doi.org/10.1002/2015GL065497, 2015.

Fujiyoshi, Y.: Melting Snowflakes, J. Atmos. Sci., 43, 307–311, https://doi.org/10.1175/1520-0469(1986)043<0307:MS>2.0.CO;2, 1986.

Di Girolamo, P., Summa, D., Cacciani, M., Norton, E. G., Peters, G., and Dufournet, Y.: Lidar and radar measurements of the melting layer: Observations of dark and bright band phenomena, Atmos. Chem. Phys., 12, 4143–4157, https://doi.org/10.5194/ACP-12-4143-2012, 2012.

Goenka, R., Anoop, S., and Ramana, M. V.: Characteristics of Precipitation Over the Southern Ocean Using Micro Rain Radar and its Comparison with Space-Based Measurements, Journal of the Indian Society of Remote Sensing, 51, 1619–1630, https://doi.org/10.1007/S12524-023-01727-8, 2023.

Heymsfield, A. J., Bansemer, A., Poellot, M. R., and Wood, N.: Observations of Ice Microphysics through the Melting Layer, J. Atmos. Sci., 72, 2902–2928, https://doi.org/10.1175/JAS-D-14-0363.1, 2015.

Hosseini, H.: Radial bright-band detection (v1.0.3), https://doi.org/10.5281/zenodo.24295740, Zenodo, 2026.

https://doi.org/10.5194/egusphere-2026-7174
Preprint. Discussion started: 24 November 2026
© Author(s) 2026. CC BY 4.0 License.

Hosseini, H., Hashemi, H., Olsson, J., Thorndahl, S. L., Rydberg, B., Körnich, H., and Berndtsson, R.: Snow transitions to rain: A review of atmospheric melting layer studies using micro rain radar and complementary approaches, Atmos. Res., 326, 108307, https://doi.org/10.1016/J.ATMOSRES.2025.108307, 2025.

Hosseini, S. H., Hashemi, H., Olsson, J., Aspegren, H., and Berndtsson, R.: Melting layer prediction via surface weather and its correlation with classes of rainfall rate, in: 12th International Workshop on Precipitation in Urban Areas, 2023.

Ikeda, K., Brandes, E. A., and Rasmussen, R. M.: NOTES AND CORRESPONDENCE: Polarimetric Radar Observation of Multiple Freezing Levels, J. Atmos. Sci., 62, 3624–3636, https://doi.org/10.1175/JAS3556.1, 2005.

Kollias, P. and Albrecht, B.: Why the melting layer radar reflectivity is not bright at 94 GHz, Geophys. Res. Lett., 32, https://doi.org/10.1029/2005GL024074, 2005.

Konjari, P., Rolf, C., Krämer, M., Afchine, A., Spelten, N., Bartolome Garcia, I., Miltenberger, A., Emig, N., Joppe, P., Schneider, J., Li, Y., Petzold, A., Bozem, H., and Hoor, P.: Stratospheric Hydration and Ice Microphysics of a Convective Overshoot Observed during the TPEx Campaign over Sweden, EGUsphere, 1–27, https://doi.org/10.5194/EGUSPHERE-2025-2847, 2025.

Martner, B. E., Neiman, P. J., and White, A. B.: Collocated Radar and Radiosonde Observations of a Double-Brightband Melting Layer in Northern California, Mon. Weather Rev., 135, 2016–2024, https://doi.org/10.1175/MWR3383.1, 2007.

Michelson, D. B., Lewandowski, R., Szewczykowski, M., Beekhuis, H., and Haase, G.: EUMETNET OPERA 6 Work Package OD5 EUMETNET OPERA weather radar information model for implementation with the HDF5 file format Version 2.4.1, https://www.eumetnet.eu/wp-content/uploads/2024/10/ODIM_H5_v2.4.1_final.pdf (last access: 13 December 2025), 2024.

Mitra, S. K., Vohl, O., Ahr, M., and Pruppacher, H. R.: A Wind Tunnel and Theoretical Study of the Melting Behavior of Atmospheric Ice Particles. IV: Experiment and Theory for Snow Flakes, J. Atmos. Sci., 47, 584–591, https://doi.org/10.1175/1520-0469(1990)047<0584:AWTATS>2.0.CO;2, 1990.

Norin, L.: Observations of anomalous propagation over waters near Sweden, Atmos. Meas. Tech., 16, 1789–1801, https://doi.org/10.5194/amt-16-1789-2023, 2023.

Petersson Wårdh, L., Hosseini, H., van de Beek, R., Andersson, J. C. M., Hashemi, H., and Olsson, J.: Have you ever seen the rain? Observing a record convective rainfall with national and local monitoring networks and opportunistic sensors, Atmos. Meas. Tech., 19, 461–483, https://doi.org/10.5194/AMT-19-461-2026, 2026.

Pfaff, T., Engelbrecht, A., and Seidel, J.: Detection of the bright band with a vertically pointing k-band radar, Meteorologische Zeitschrift, 23, 527–534, https://doi.org/10.1127/metz/2014/0605, 2014.

Poirier, É., Thériault, J. M., and Leriche, M.: Role of sublimation and riming in the precipitation distribution in the Kananaskis Valley, Alberta, Canada, Hydrol. Earth Syst. Sci., 23, 4097–4111, https://doi.org/10.5194/HESS-23-4097-2019, 2019.

Rajasekharan Nair, H.: Discernment of near-oceanic precipitating clouds into convective or stratiform based on Z–R model over an Asian monsoon tropical site, Meteorology and Atmospheric Physics, 132, 377–390, https://doi.org/10.1007/S00703-019-00696-3, 2019.

https://doi.org/10.5194/egusphere-2026-7174
Preprint. Discussion started: 24 November 2026
© Author(s) 2026. CC BY 4.0 License.



Raut, B. A., Konwar, M., Murugavel, P., Kadge, D., Gurnule, D., Sayyed, I., Todekar, K., Malap, N., Bankar, S., and Prabhakaran, T.: Microphysical Origin of Raindrop Size Distributions During the Indian Monsoon, Geophys. Res. Lett., 48, e2021GL093581, https://doi.org/10.1029/2021GL093581, 2021.

Sanchez-Rivas, D. and Rico-Ramirez, M. A.: Detection of the melting level with polarimetric weather radar, Atmos. Meas. Tech., 14, 2873–2890, https://doi.org/10.5194/amt-14-2873-2021, 2021.

Schauwecker, S., Rohrer, M., Huggel, C., Endries, J., Montoya, N., Neukom, R., Perry, B., Salzmann, N., Schwarb, M., and Suarez, W.: The freezing level in the tropical Andes, Peru: An indicator for present and future glacier extents, Journal of Geophysical Research: Atmospheres, 122, 5172–5189, https://doi.org/10.1002/2016JD025943, 2017.

Song, J. I., Yum, S. S., Park, S., Kim, K., Park, K., and Joo, S.: Climatology of Melting Layer Heights Estimated From Cloud Radar Observations at Various Locations, Journal of Geophysical Research: Atmospheres, 126, https://doi.org/10.1029/2021JD034816, 2021.

Wang, H., Lei, H., and Yang, J.: Microphysical processes of a stratiform precipitation event over eastern China: analysis using micro rain radar data, Adv. Atmos. Sci., 34, 1472–1482, https://doi.org/10.1007/S00376-017-7005-6, 2017.

Wang, H., Wang, W., Wang, J., Gong, D., Zhang, D., Zhang, L., and Zhang, Q.: Rainfall Microphysical Properties of Landfalling Typhoon Yagi (201814) Based on the Observations of Micro Rain Radar and Cloud Radar in Shandong, China, Adv. Atmos. Sci., 38, 994–1011, https://doi.org/10.1007/s00376-021-0062-x, 2021.

Zhang, J., Howard, K., Langston, C., Kaney, B., Qi, Y., Tang, L., Grams, H., Wang, Y., Cocks, S., Martinaitis, S., Arthur, A., Cooper, K., Brogden, J., and Kitzmiller, D.: Multi-Radar Multi-Sensor (MRMS) Quantitative Precipitation Estimation: Initial Operating Capabilities, Bull. Am. Meteorol. Soc., 97, 621–638, https://doi.org/10.1175/BAMS-D-14-00174.1, 2016.

Zhou, L., Zhou, Y., Fu, Z., Lü, J., Lu, C., and Xiao, H.: Vertical structures and microphysical mechanisms of winter precipitation over the southwestern mountainous area of China, Atmos. Res., 303, 107346, https://doi.org/10.1016/J.ATMOSRES.2024.107346, 2024.

Zhu, Z., Qi, Y., Zhao, Z., and Li, F.: How Do Wavebands Affect the Accuracy of Radar QPE?, SSRN: https://ssrn.com/abstract=5976155, https://doi.org/10.2139/ssrn.5976155, 2025.

BALTRAD · GitHub, https://github.com/baltrad, last access: 13 December 2025., 2025.

numpy.gradient — NumPy v2.2 Manual, https://numpy.org/doc/2.2/reference/generated/numpy.gradient.html, last access: 25 February 2026., 2026.